Computers & Structures Vol. 25, No. 6, pp. 845–869, 1987
Printed in Great Britain.

0045-7949/87 $3.00 + 0.00

NONLINEAR ANALYSIS OF REINFORCED CONCRETE PLATE AND SHELL STRUCTURES USING 20-NODED ISOPARAMETRIC BRICK ELEMENTS

M. CERVERA, E. HINTON and O. HASSAN
University College of Swansea, Swansea SA2 8PP, U.K.

(*Received* 18 *August* 1986)

Abstract—This paper describes an efficient and accurate, 3-D finite element model which may be adopted in the nonlinear analysis of reinforced concerete plate and shell structures. Benchmark tests are undertaken to check the computational model.

INTRODUCTION

Computer-aided structural analysis of reinforced concrete structures has been the object of extensive research for almost 20 years. Attention first focused on 2-D and axisymmetric models, but it was soon widened to include plate and shell systems. Problems involving reinforced concrete shells are of great practical interest, as they include those that appear in nuclear engineering, gas storage tanks, etc.

The usual method of modelling reinforced concrete shell structures is to make use of the so-called "layered" shell elements. The elements are composed of a series of through-thickness "layers", each assumed to be in a state of plane stress. This approach has several disadvantages:

(a) The quadrature rule used to integrate quantities such as the residual forces and the tangential stiffness through the thickness (i.e. the mid-ordinate rule) is not very accurate, and many layers (8–12) must be used to ensure reasonable accuracy.

(b) The large number of sampling points used per element makes the evaluation of the tangential stiffness matrix and internal force vector quite expensive.

(c) The plane stress assumption in the layered plate or shell implies that the normal stress perpendicular to the midsurface is neglected. Furthermore, in most models, in-plane stresses are treated separately from transverse shear stresses, usually in an inconsistent way.

(d) Cracks are assumed to form due to in-plane stresses only, the effect of the transverse shear stresses being disregarded when checking for cracking. As a result, cracks are perpendicular to the midsurface, which is an unrealistic constraint on the model that makes it unable to represent non-flexural failures.

(e) The elements used are usually of the Mindlin-type. This results in an *a priori* imposed uniform distribution of transverse shear strains through the thickness.

(f) Concrete slabs are usually moderately thick, so consideration of transverse shear strains and stresses is not insignificant, especially near the supports.

All these considerations point to the necessity of developing fully 3-D models which can be used to analyse reinforced concrete structures both efficiently and accurately.

The use of a standard 3-D approach for the analysis avoids the complexities associated with shell formulations, allows for a wider range of applications, and is free from the simplifying assumptions mentioned above. On the other hand, a 3-D analysis usually involves a larger number of degrees of freedom for a given discretization than a shell formulation, and requires better mesh-generation and post-processing facilities than those of an essentially 2-D analysis.

This paper reviews our efforts to develop such a 3-D model for nonlinear structural analysis of reinforced concrete structures subjected to short-term static loading.

THREE-DIMENSIONAL COMPUTATIONAL MODEL

The 3-D computational model is now described. First, the finite element discretization is discussed, with particular attention given to the type of integration rule adopted and problems of locking behaviour. Next, the constitutive models adopted are presented.

Finite element model

Concrete solid. Although other choices are available for 3-D analysis in the present work we adopt the 20-node isoparametric element shown in Fig. 1. Hierarchical, rather than standard, interpolation functions [1] are used in the present formulation. Trilinear shape functions are used for the eight corner nodes and quadratic hierarchical shape functions are employed for the 12 mid-side nodes. The use of this hierarchical approach provides a "natural" preconditioning matrix when iterative solution techniques (such as the conjugate gradient method) are used. Furthermore, hierarchically derived stiffness matrices are better conditioned than the standard ones. This feature is of additional advantage when analysing plates and shells with 3-D elements.

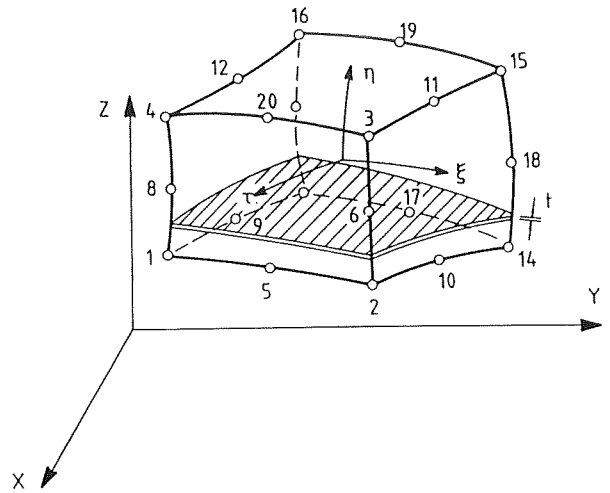

Fig. 1. Twenty-noded, isoparametric solid element with reinforcement.

Isoparametric finite elements are highly effective in practice, although for linear problems a considerable proportion of the total computational effort is often absorbed in the numerical integration of the stiffness matrix coefficients. It is thus very important to choose suitable integration schemes that are both accurate and computationally efficient.

For nonlinear problems the previous observation is even more critical since evaluation of the stiffness matrix occurs frequently. Equally important, the integration points are also the sampling points for the stresses and material state determination. These points are used, in turn, in the evaluation of the internal resisting forces. On one hand, the use of few sampling points reduces the computation time, but on the other, the use of more stress sampling points provides more complete information about the material state throughout the element. Clearly, a compromise is to be sought.

Usually, either Gauss–Legendre or Lobatto product rules are used with linear and quadratic solid elements. Gauss quadratures are more accurate, while Lobatto rules possess the advantage of having sampling points on the element faces, where the peak stresses usually occur.

The $2 \times 2 \times 2$ and $3 \times 3 \times 3$ Gaussian product rules exactly integrate the stiffness matrix of the 8-noded and 20-noded elements (for elements with constant Jacobian and with constant material properties throughout the element), respectively. Reduced integration is here defined as the use of $1 \times 1 \times 1$ and $2 \times 2 \times 2$ rules for 8-noded and 20-noded elements respectively.

Reduced integration is computationally attractive, because it greatly reduces the number of operations to perform in the evaluation of the residual forces and tangential stiffness matrices. However, it is well known that under-integrated matrices are rank deficient. This defect can lead to the development of spurious deformation mechanisms that affect the behaviour of a single element and may, for certain meshes, propagate throughout the mesh. Much effort has been devoted to the development of "stabilization" or "mechanism suppression" techniques [2, 3] that can be used at the element level to suppress the spurious mechanisms. As a result, highly efficient 8-noded elements with only one integration point are available.

Results presented by Crisfield [4] show that spurious mechanisms are more likely to occur where cracking or material softening is considered. Under-integration may seriously affect the computed results if material nonlinearity is to be considered.

In the present work, a different set of integration rules, first introduced by Irons [5], is used for the 20-noded element. These rules have proved to be both accurate and efficient [6].

The present Gaussian-type rules are designed to integrate complete polynomials. They correctly integrate polynomials of the type $\Sigma C_{ijk} x^i y^j z^k$ (with $i+j+k \leqslant n$) while product Gauss rules integrate correctly more terms, so that $i, j, k \leqslant n$—an unnecessary accuracy. When these rules are used to integrate the stiffness matrix of the 20-noded element, no rank deficiency is observed. Furthermore, use of these rules alleviates the overstiff behaviour observed when the $3 \times 3 \times 3$ rule is employed.

The rules can be expressed in the form

$$\begin{aligned}\int_{-1}^{+1}\int_{-1}^{+1}\int_{-1}^{+1} f(x,y,z)\,dx\,dy\,dz \\ = A_1 f(0,0,0)\ (1\text{ term}) + B_6[f(-b,0,0) \\ + f(b,0,0) + f(0,-b,0)\ldots 6\text{ terms}] \\ + C_8[f(-c,-c,-c) + f(c,-c,-c) \\ + \ldots 8\text{ terms}]. \end{aligned} \quad (1)$$

The coefficients in (1) for the different rules are:

	A	B	C	b	c
Rule 14	0.000000	0.886477	0.335180	0.795822	0.758787
Rule 15a	1.564444	0.355556	0.537778	1.000000	0.674100
Rule 15b	0.712137	0.396312	0.396312	0.848418	0.727662

The distribution of the sampling points over the volume of the element can be seen in Fig. 2.

Rule 15a has the advantage of having sampling points at the centres of the element faces. These locations are convenient sampling positions for the stress peak values. Furthermore, the mismatch between the stress values at these points for two

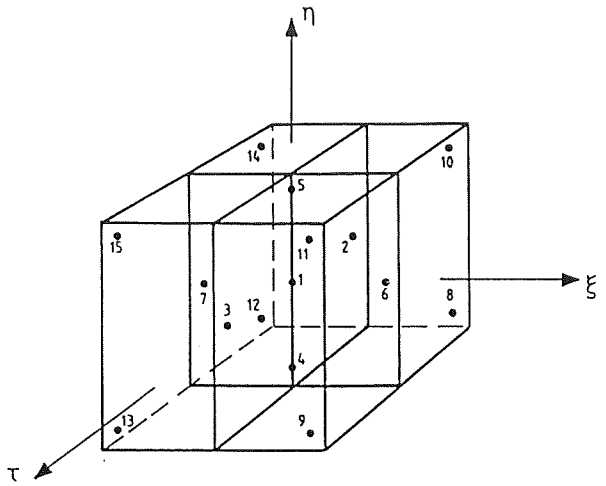

Fig. 2. Distribution of the integration points over the element volume.

adjoining elements gives an estimate of the accuracy of the adopted mesh.

As the solid finite element is intended for use in the analysis of plates and shells of various thicknesses, some linear elastic aspect ratio tests were carried out. A series of uniformly loaded square plates of various span-to-thickness ratios, a/h, were analysed with two sets of boundary conditions: (1) simply supported on all edges, and (2) clamped conditions on all edges.

Symmetric quadrants, idealized with regular meshes of 4, 9 and 16 elements, were used for the analyses, and plots of normalized central deflection against $\log(a/h)$ for the individual elements are shown in Figs 3 and 4 for the two different boundary conditions, respectively. The central displacements are divided by the value predicted by thin plate theory. The solutions for the solid elements should become asymptotic to the thin plate solution as the aspect ratio, a/t, increases.

Figure 3(a) shows results for the simply supported plate using the integration rule 15a for the three different meshes. A locking-type behaviour is exhibited, but as expected, the problem is greatly alleviated by refinement of the mesh. Figures 3(b) and (c) show results for the same problem comparing the performance of the proposed rule against the classical $2 \times 2 \times 2$ and $3 \times 3 \times 3$ Gaussian rules for the 9- and 16-element meshes, respectively. It can be observed that the 15-point rule, besides being computationally more economical than the equivalent "exact" Gaussian rule, is less prone to locking. The results corresponding to the $2 \times 2 \times 2$ rule show the benefits of reduced integration in alleviating locking behaviour. Although the $2 \times 2 \times 2$ rule gives better results than the two other "exact" rules, for very thin situations an oscillation in the lateral displacements was observed due to a spurious low-energy mode. The $2 \times 2 \times 2$ rule will not be used in this work for nonlinear analysis for this reason and because the spread of points throughout the element is thought to be insufficient for nonlinear material analysis.

Figure 4 shows similar results for the clamped plate. In this case the locking behaviour is more severe, and the previous conclusions are confirmed.

The reason for this locking behaviour is clear. The transverse shear stresses are defined (up to the first-order terms) as

$$\gamma_{xz} = \frac{\partial u}{\partial z} + \frac{\partial w}{\partial x}$$

$$\gamma_{yz} = \frac{\partial v}{\partial z} + \frac{\partial w}{\partial y}. \tag{2}$$

With the quadratic shape functions used for the element, the displacements u, v and w are expressed as second-order polynomials on x, y and z. Consequently, the terms $\partial u/\partial z$ and $\partial v/\partial z$ are quadratic in x and y, while the terms $\partial w/\partial x$ and $\partial w/\partial y$ are only linear in x and y, respectively. Therefore, due to the different order of the terms involved, it is impossible for the strains γ_{xz} and γ_{yz} to vanish for all points within the element, as they should in thin-plate situations. The spurious shear strains are responsible for the shear-locking behaviour exhibited.

From a careful analysis of these and other results it appears wise to limit the aspect ratio of individual 20-node brick elements to a maximum of about 25 when bending action predominates and when adequate computational precision (at least 11 significant digits) is available.

Reinforcement representation. Analysis of reinforced concrete structures by the finite element method requires a simple yet accurate way of representing the reinforcement.

In this work, concrete and reinforcement are represented with a single element [7, 8]. Perfect bond is assumed between the reinforcement and the surrounding concrete. The stiffness and internal forces associated with the reinforcement are integrated and added to those of the concrete to get the total stiffness and internal forces of the element.

Each set of reinforcing bars is smeared as a 2-D membrane "layer" of equivalent thickness (and hence equal area). The layer is placed inside the solid element to coincide with the surface corresponding to (ξ, η, const.), (ξ, const., τ) or (const., η, τ) as appropriate. The resulting element is shown in Fig. 1.

Although this procedure does not allow the consideration of reinforcement in an arbitrary position inside the element, it covers most of the practical situations. The proposed restriction has the advantage of an easy definition of the sampling points used to perform the necessary surface integrations over the steel membrane.

Reinforcing bars are assumed to resist only axial stresses in the bar direction. A local Cartesian coordinate system must be set up at each integration point in the reinforcing membrane with one of the axes pointing along the bar direction. Stresses and the local stiffness matrix for the reinforcement are first

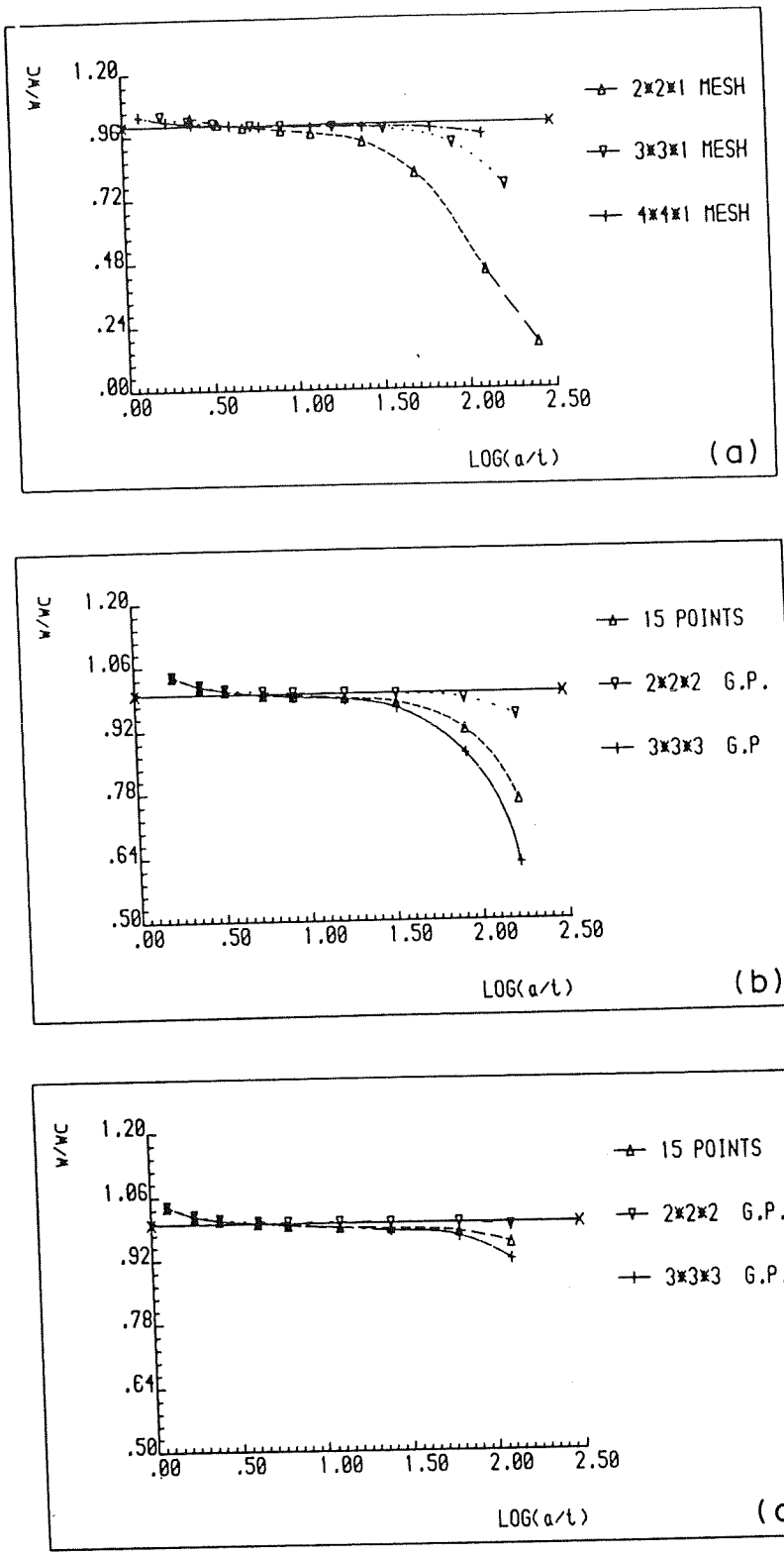

Fig. 3. Aspect ratio tests—simply supported, uniformly loaded plate: (a) 15-point rule for $2 \times 2 \times 1$, $3 \times 3 \times 1$ and $4 \times 4 \times 1$ meshes, (b) $3 \times 3 \times 1$ mesh with 15-point, $2 \times 2 \times 2$ and $3 \times 3 \times 3$ integration rules and (c) $4 \times 4 \times 1$ mesh with 15-point, $2 \times 2 \times 2$ and $3 \times 3 \times 3$ integration rules.

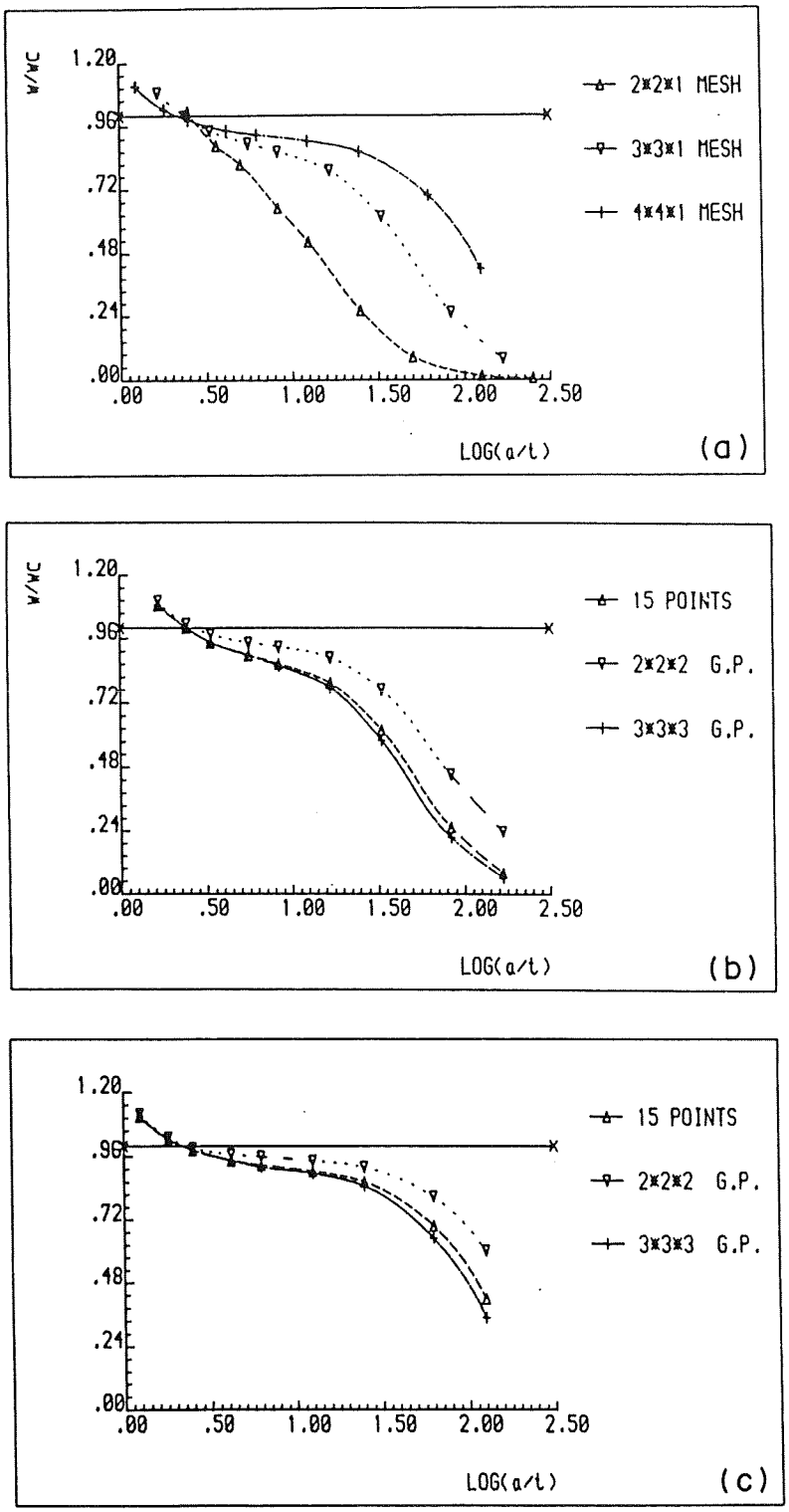

Fig. 4. Aspect ratio tests—clamped, uniformly loaded plate: (a) 15-point rule for $2 \times 2 \times 1$, $3 \times 3 \times 1$ and $4 \times 4 \times 1$ meshes, (b) $3 \times 3 \times 1$ mesh with 15-point, $2 \times 2 \times 2$ and $3 \times 3 \times 3$ integration rules and (c) $4 \times 4 \times 1$ mesh with 15-point, $2 \times 2 \times 2$ and $3 \times 3 \times 3$ integration rules.

evaluated in this local system, and then transformed into the global system. Finally, the contribution of the bar is added to that of the solid concrete.

The local system can be defined in two stages. First, an auxiliary system is set up so that the x- and y-axes are tangential to the membrane and are mutually orthogonal, and the z-axis is normal to both the x- and y-axes. Then, the local system is obtained by rotating the auxiliary system about its z-axis so that the x-axis coincides with the bar direction. Different possibilities exist for the construction of the auxiliary system. In particular cases, such as plates, it can coincide with the global system, or be constructed as a local polar system, pointing in the radial, circumferential and vertical directions. In a more general situation, this system can be set up using the terms of the Jacobian matrix of the sampling point under consideration. This matrix provides three vectors, each of them tangential to one of the natural coordinate axes of the element. Because of the procedure adopted to place the reinforcement inside the element, two of these vectors will always be tangential to the reinforcing membrane, and they can be used to construct the auxiliary Cartesian system using a simple orthogonalization procedure.

Constitutive models

The constitutive models employed here account for various types of material nonlinearities in the concrete and steel. The material behaviour is assumed to be independent of time.

Material modelling of uncracked concrete. Experimental evidence indicates that the stress–strain relationship for concrete is nonlinear even for low stress levels. The plasticity models seem to provide an adequate basis for describing the inelastic deformation of concrete without involving the difficulties of the fracturing and endochronic theories, and requiring fewer material parameters to be defined. In the present model linear elasticity is used for the recoverable part of the strain, and a work-hardening plasticity approach is employed for the irrecoverable part of the deformation.

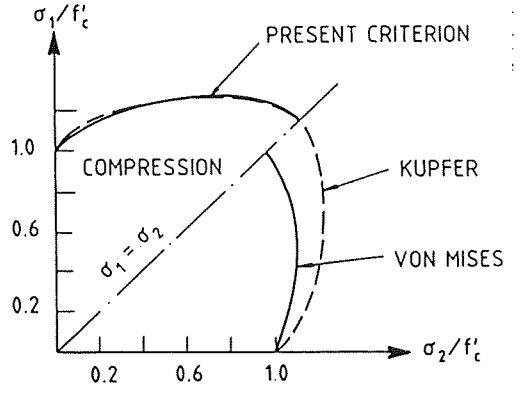

Fig. 5. Comparison of present yield surface with experimental results.

A hardening–plasticity model requires the full description of the following items: (i) a yield condition, (ii) a flow rule, (iii) a hardening rule, and (iv) a crushing condition.

(i) *The yield criterion.* Under a triaxial stress state the yield criterion for concrete is generally assumed to be dependent on the three stress invariants. Nevertheless, a yield function depending only on the first (I_1) and second (J_2) stress invariants can be an adequate assumption for most practical situations. The yield criterion adopted here is of such a type [9], and it can be written in the form

$$f(I_1, J_2) = [\alpha I_1 + 3\beta J_2]^{1/2} = \sigma_o, \tag{3}$$

where α and β are two material parameters and σ_0 is the equivalent effective stress.

It can be noted that the Huber–Mises yield condition can be recovered by using $\alpha = 0.0$ and $\beta = 1.0$.

The parameters α and β can be obtained from biaxial experimental results. If Kupfer's results [10] are to be fitted for the principal stress ratios $\sigma_1/\sigma_2 = \infty$ (uniaxial compression test) and $\sigma_1/\sigma_2 = 1.0$ (equal biaxial compression test) the values obtained are

$$\alpha = 0.355\,\sigma_0 \quad \text{and} \quad \beta = 1.355.$$

The resulting yield criterion is compared in Fig. 5 with the experimental failure envelope of [10].

The yield criterion in (3) defines a surface in the stress space. It does not depend on the third stress invariant, so it has circular traces on the deviatoric planes. Because of the quadratic dependence on the first invariant, the meridians are parabolic.

The yield criterion can be used as the basis for an elastic–perfectly plastic model if σ_0 is taken to be equal to the ultimate compressive stress f'_c obtained from uniaxial compression tests. In such a model the response is elastic until the effective stress reaches the value of f'_c. After that concrete flows until the crushing surface is reached in the strain space.

It is more realistic to use a hardening model in which σ_0 is a function of a hardening parameter. A value $\sigma_0 = \alpha_1 f'_c$ defines the initial yield surface, which limits the elastic behaviour. When this surface is reached inelastic deformation begins, and a hardening rule monitors the expansion of the yield surface under further loading. In this way, a whole family of "loading surfaces" is defined, as shown in Fig. 6. Unloading inside the current loading surface occurs elastically. Under loading, the loading surfaces expand until either the failure surface ($\sigma_0 = f'_c$) or, the crushing surface (in the strain space) is reached.

(ii) *The flow rule.* In plasticity theory a flow rule is defined so that the increments of plastic strain can be evaluated from a given stress state.

Although very little supportive experimental evidence is available, an associative flow rule will be employed here. This means that the plastic deform-

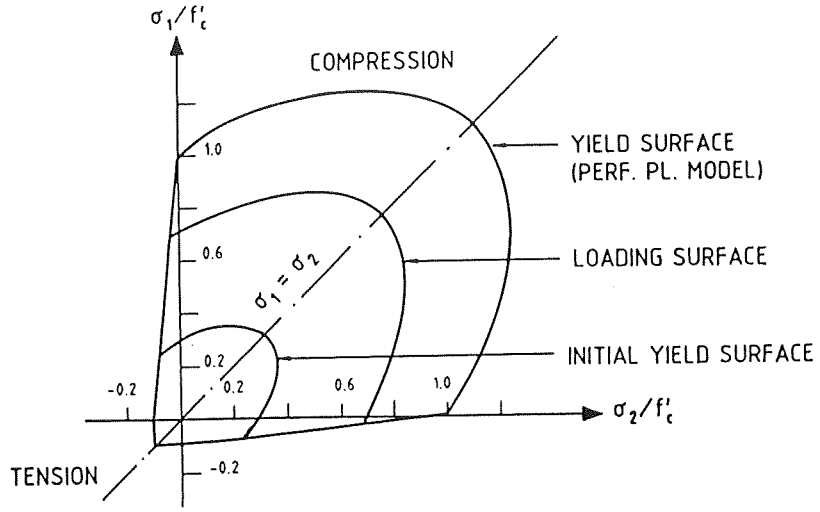

Fig. 6. Loading surfaces for concrete constitutive model.

ation rate vector will be assumed to be normal to the adopted yield surface. The plastic strain increment is the defined as [11]

$$d\epsilon^p = d\lambda\, \partial f(\sigma)/\partial\sigma = d\lambda\, \mathbf{a}, \tag{4}$$

where $d\lambda$ is a factor determining the size of the plastic strain increment and $\partial f/\partial\sigma$ is a vector normal to the current loading surface.

Equation (4) can be rewritten as

$$f(\sigma) = [2c\sigma_0 I_1 + 3\beta J_2]^{1/2} = \sigma_0, \tag{5}$$

with $c = \alpha/2\sigma_0$. This can be solved for σ_0, giving

$$f(\sigma) = cI_1 + (c^2 I_1 + 3\beta J_2)^{1/2} = \sigma_0. \tag{6}$$

The flow vector **a** can now be computed as

$$\mathbf{a}^T = \left[\frac{\partial f}{\partial\sigma_x}, \frac{\partial f}{\partial\sigma_y}, \frac{\partial f}{\partial\sigma_z}, \frac{\partial f}{\partial\tau_{xy}}, \frac{\partial f}{\partial\tau_{yz}}, \frac{\partial f}{\partial\tau_{zx}}\right]$$

$$a_1 = c + [2(c^2+\beta)\sigma_x + (2c^2-\beta)(\sigma_y+\sigma_z)]/\Delta$$

$$a_2 = c + [2(c^2+\beta)\sigma_y + (2c^2-\beta)(\sigma_z+\sigma_x)]/\Delta$$

$$a_3 = c + [2(c^2+\beta)\sigma_z + (2c^2-\beta)(\sigma_x+\sigma_y)]/\Delta$$

$$a_4 = 6\beta\,\tau_{xy}/\Delta$$

$$a_5 = 6\beta\,\tau_{yz}/\Delta$$

$$a_6 = 6\beta\,\tau_{zx}/\Delta, \tag{7}$$

where

$$\Delta = 2[(c^2+\beta)(\sigma_x^2+\sigma_y^2+\sigma_z^2) + (2c^2-\beta)(\sigma_x\sigma_y+\sigma_y\sigma_z+\sigma_z\sigma_x) + 3\beta(\tau_{xy}^2+\tau_{yz}^2+\tau_{zx}^2)]^{12}.$$

The plastic multiplier can be found to be [11]

$$d\lambda = \frac{1}{H' + \mathbf{a}^T\mathbf{D}\mathbf{a}}\,\mathbf{a}^T\mathbf{D}\,d\varepsilon, \tag{7a}$$

where H' is the hardening parameter, **D** is the elasticity matrix, and $d\varepsilon$ is the total strain incremental vector.

The complete elasto-plastic incremental stress–strain relationship is given by [11]

$$d\sigma = \mathbf{D}_{ep}\,d\varepsilon \tag{8}$$

with the elasto-plastic material matrix defined by

$$\mathbf{D}_{ep} = \mathbf{D} - \frac{\mathbf{D}\mathbf{a}^T\mathbf{a}\mathbf{D}}{H' + \mathbf{a}^T\mathbf{D}\mathbf{a}}. \tag{9}$$

(iii) *The hardening rule.* The hardening rule defines the motion of the loading surfaces during plastic deformation. A relationship between the accumulated plastic strain and the effective stress σ_0 is assumed. In this way, the concepts of effective plastic strain and effective stress allow for extrapolation of results from uniaxial tests to the multiaxial situation.

In the present work, such a relationship is assumed to be the conventional "Madrid Parabola" [9]

$$\sigma_0 = E_0\varepsilon - \frac{1}{2}\frac{E_0}{\varepsilon_0}\varepsilon^2, \tag{10}$$

where σ_0 is the effective stress, E_0 is the initial Young's modulus, ε is the current total strain, and ε_0 is the total strain at peak stress f_c'.

Substituting the elastic strain $\varepsilon_e = \sigma_0/E_0$ in (10), the desired relation is obtained:

$$\sigma_0 = -E_0\varepsilon_p + (2E_0^2\varepsilon_0\,\varepsilon_p)^{1/2} \quad \alpha_1 f_c' \leqslant \sigma_0 \leqslant f_c'. \tag{11}$$

From (11) the hardening parameter can be obtained

$$H' = \frac{d\sigma_0}{d\varepsilon} = E_0[(\varepsilon_0/2\varepsilon_p)^{1/2} - 1]. \tag{12}$$

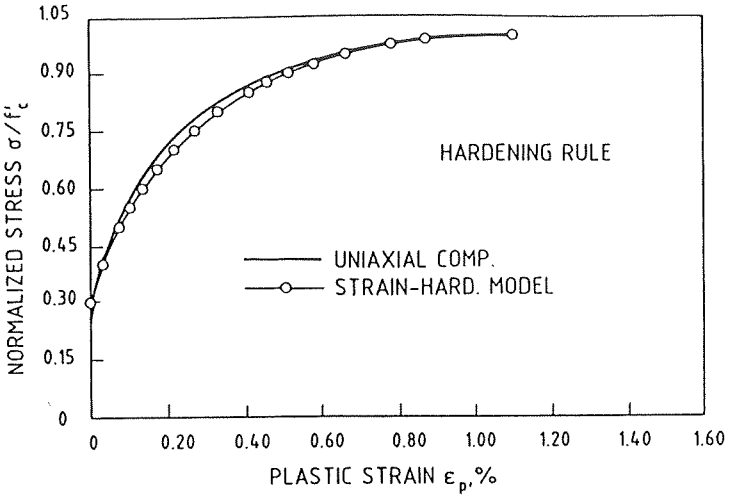

Fig. 7. Comparison of hardening rules with the inelastic uniaxial compressive strains of Kupfer.

As can be seen in Fig. 7, very good agreement is obtained with the experimental results in [10], by taking

$$\alpha_1 = 0.3 \quad \text{and} \quad \varepsilon_0 = 2f'_c/E_0.$$

(iv) *The crushing condition.* The hardening–plastic model described above governs the increase of the inelastic deformation in concrete under compressive stress. Inelastic deformation continues in the concrete until crushing occurs. The crushing type of fracture is a strain-controlled phenomenon. A failure surface in the strain space must be defined so that this kind of fracture can be taken into account. A simple way of doing so, despite the lack of experimental data on concrete ultimate deformation capacity under multiaxial loading, is to assume a crushing surface in the strain space whose size is related to a maximum equivalent strain extrapolated from uniaxial tests. The following failure surface may be used:

$$3J'_2 = \varepsilon_u^2, \tag{13}$$

where J'_2 is the second deviatoric strain invariant and ε_u is an ultimate total strain value obtained from uniaxial tests. When concrete reaches the crushing surface it is assumed to release all stresses and lose its stiffness.

Numerical modelling of cracked concrete. Probably the main feature of plain concrete material behaviour is its low tensile strength, which results in tensile cracking at very low stress compared with the failure stress in compression.

A smeared crack model will be adopted in this work. To be fully described such a model requires the following items: (i) a cracking criterion, (ii) a strain-softening (or tension-stiffening) rule, and (iii) a model for shear transfer.

(i) *Cracking criterion.* The tensile strength of uncracked plain concrete can be obtained from laboratory tests. This facility is not available to a designer, however. In design, concrete properties are usually deduced from the compressive strength. In the presence of reinforcing steel the prediction of crack initiation and crack direction is even more difficult. Simple criteria are therefore favoured by most analysts to predict tensile fracture. Usually, a maximum tensile stress or maximum tensile strain criterion is used for this purpose.

In the present work, concrete in tension is modelled as a linear elastic-strain softening material and the maximum tensile stress criterion will be employed to distinguish elastic behaviour from tensile fracture. For a previously uncracked sampling point, the principal stresses and their directions are evaluated. If the maximum principal stress exceeds a limiting value, a crack is formed in a plane orthogonal to the offending stress. Thereafter, the behaviour of the concrete is no longer isotropic—it becomes orthotropic, and the local material axes coincide with the principal stress directions. It should be noted that the direction of the crack remains fixed thereafter—this is known as the fixed crack approach.

A maximum of two sets of cracks are allowed to form at each sampling point. For simplicity, the crack directions must be orthogonal.

Under further loading, secondary cracking may occur at a sampling point that was originally cracked in one direction. Three possibilities may be followed to determine the direction of the second set of cracks:

(a) The principal material axes can be rotated to coincide with the current principal stress (or strain) directions. This is known as the rotating crack model [12]. Although this approach is reported to produce results which are in good agreement with experimental results, the model could be physically objectionable since it implies rotation of defects within the material [13].

(b) The material axes are fixed in the directions corresponding to the principal stress directions when the primary cracks occurred, irrespective of the possible rotation of the stresses.

(c) By keeping the direction of the first set of cracks fixed, a search is performed to determine the maximum stress in the plane parallel to the existing crack.

For this computation only the normal and shear stresses acting on that plane are considered. If this maximum stress exceeds the limiting value, then a new set of cracks is formed perpendicular to it, and the local material axes are fixed. This is the option that will be used here.

The limiting value required to define the onset of cracking is established as follows:

(i) in the triaxial tension zone,

$$\sigma_{i0} = f'_t \quad i = 1, 2, 3, \tag{14}$$

as there is experimental evidence that triaxial tensile strength of concrete is almost independent of the stress ratio.

(ii) for tension–tension–compression and tension–compression–compression stress states, linearly decreasing tensile strength expressions are used,

$$\sigma_{i0} = f'_t\left(1 + \frac{\sigma_{i+1}}{f'_c}\right) \qquad \sigma_{i+1} \leqslant 0 \tag{15}$$

$$\sigma_{i0} = f'_t\left(1 + \frac{\sigma_{i+1}}{f'_c}\right)\left(1 + \frac{\sigma_{i+2}}{f'_c}\right) \qquad \sigma_{i+1}, \sigma_{i+2} \leqslant 0. \tag{16}$$

These expressions incorporate the fact that compression in one direction favours microcracking in the orthogonal directions, thus reducing tensile capacity.

The resulting cracking surfaces are shown in Fig. 8.

(ii) *Strain-softening rule.* The first studies done on numerical analysis of reinforced concrete structures assumed concrete to be elastic–brittle in tension. When cracking occurred, the stress normal to the crack direction was immediately released and dropped to zero. It was soon discovered that this procedure leads to great convergence difficulties, and more importantly, to results that depend strongly on the size of the finite elements used in the analysis.

It was then argued that due to bond forces, cracked concrete carries between the cracks a certain amount of tensile stress normal to the cracked plane. The concrete adheres to the reinforcing bars and contributes actively to the overall stiffness of the structure. This effect is known as tension-stiffening. It can be incorporated into the computational model in two indirect ways: (a) assuming that the loss of tensile strength in concrete occurs gradually after cracking [14], or (b) modifying the steel stress–strain curve [15].

The first option is equivalent to considering concrete as an elastic-strain-softening material in tension, and has been extensively used in computational analysis of reinforced concrete structures. However, two main problems remained unsolved. The first one is that there is no objective way of measuring "how much" tension-stiffening should be included in the model. It is easy to choose a tension-stiffening curve that will adequately fit experimental results, but very difficult to make any *a priori* predictions. Second, the effect, if explained in terms of bond interaction with the reinforcing steel, cannot be applied to plain concrete structures, or to concrete located at a certain distance from the reinforcement.

Considerable experimental research has recently been directed towards the study of the post-peak behaviour of cementitious materials. Servo-controlled testing with very stiff test devices have provided new experimental evidence which was not available earlier from predominantly load-controlled test data. Fracture mechanics models have also been applied to the study of notch-sensitive problems in plain concrete [16, 17]. These studies have shown the attractiveness of using some fracture energy concepts in the material modelling of concrete. Based on these concepts some

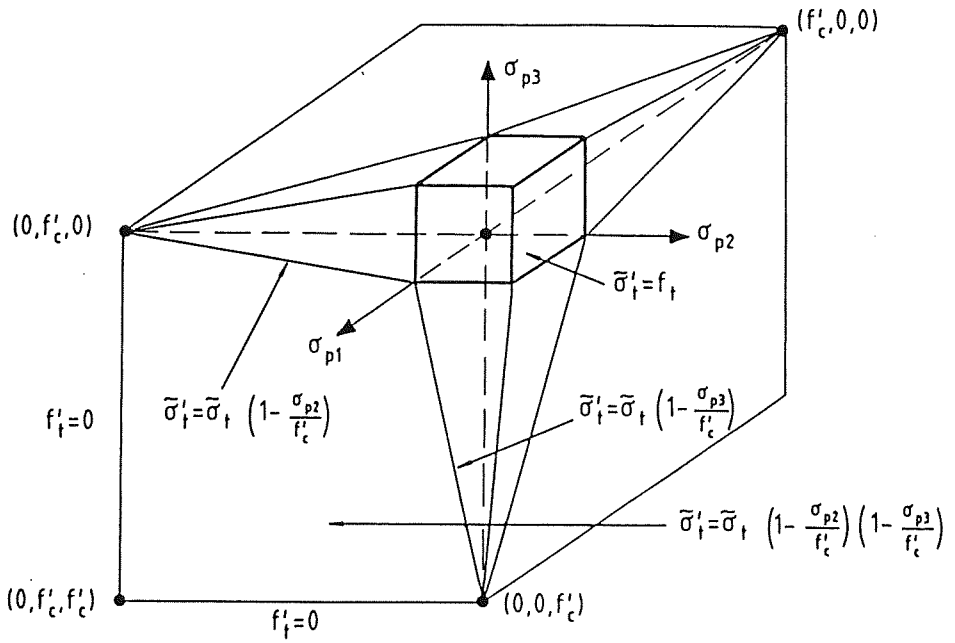

Fig. 8. Three-dimensional tensile failure envelope of concrete model.

new composite damage models have been proposed for cementitious materials such as concrete [18, 19].

The main concept borrowed from fracture mechanics to develop these models is the assumption that the fracture energy release rate, G_f, is a material property, rather than the local stress–strain curve. The implementation of the "G_f = const." concept leads to the important conclusion that the local strain-softening law depends on a characteristic length, l_c, depending on the finite element mesh. As a result, the fracture energy concept leads to a non-local format of the equivalent softening relation which is fundamentally different from the local constitutive formats of strain-softening plasticity and continuous damage mechanics [20].

In defining a curve to model the strain-softening effect, two aspects have to be considered: the shape of the adopted curve and the value of the parameters needed to define it. Different shapes of the descending branch of the stress–strain curve have been used by different authors. In most of the cases, either a simple straight line shape, or a bi-linear shape, have been used. The bi-linear shape was recommended by Petersson [21] in the context of fracture mechanics and based on experimental tests. Nonlinear curves have been used by Nilsson and Oldenburg [22], Jiang [23], Glemberg [24] and others.

The assumptions used to select the parameters defining such a curve are more important than the shape of the strain-softening curve selected. It is now widely accepted that to make the constitutive model objective with regard to the size of the finite elements used in the mesh, the softening curve must be related to the fracture energy of the concrete.

Assuming that the stress, σ, across an opening crack is a function of the crack width, w, the fracture energy is defined as

$$G_f = \int_0^\infty \sigma(w)\,\mathrm{d}w. \tag{17}$$

G_f represents the energy needed to separate the two crack surfaces. Typical values of the fracture energy for normal concretes are in the range of 50–200 N/m.

The smeared approach does not represent individual cracks, so the crack width, w, must be smeared into an equivalent crack strain, ε_c, related to the physical crack opening by a characteristic length, l_c. Nilsson [22] derived this relation considering a control volume, V, containing a crack with an area S. It is assumed that once the crack is formed, all inelastic deformation inside the control volume takes place in the crack, the rest of the volume remaining elastic.

The rate of energy dissipation in the crack is

$$\dot{\pi}_S = \int_S \sigma\,\dot{w}\,\mathrm{d}S. \tag{18}$$

Now, assume the control volume to be subjected to the same state of stress as the crack, but strained by the equivalent strain ε_c. The rate of energy dissipation in the volume is

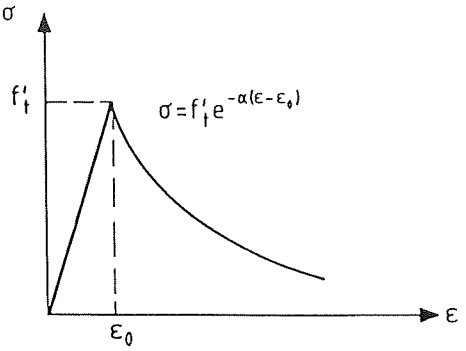

Fig. 9. Assumed strain-softening model for concrete.

$$\dot{\pi}_V = \int_V \sigma\,\dot{\varepsilon}_c\,\mathrm{d}V. \tag{19}$$

If the stress, strain and crack width are assumed to be constant inside the considered volume, then equating the rate of energy dissipation in the crack to that in the control volume gives the relationship between the crack width and the fictitious crack strain

$$w = (V/S)\,\varepsilon_c = l_c\varepsilon_c. \tag{20}$$

This relation defines the characteristic length as the ratio between the control volume and the crack surface.

In this work, an exponential function (see Fig. 9) is used to simulate the strain-softening effect, so that [22]

$$\sigma = f'_t\,[\exp[-(\varepsilon - \varepsilon_0)/\alpha]], \tag{21}$$

where f'_t is the tensile strength of concrete, ε_0 is strain at cracking, α is the softening parameter, and ε is the nominal tensile strain in the cracked zone.

The softening parameter, α, is determined by the evaluation of the integral in (17) and by the introduction of the relation between the crack opening w and the fictitious crack strain ε_c (20). This yields

$$\alpha = (G_f - \tfrac{1}{2}f'_t\varepsilon_0 l_c)/f'_t l_c > 0. \tag{22}$$

In the context of finite element computations the control volume for crack monitoring is the volume associated with a sampling point in a given element. In the present work, the characteristic length is computed for each sampling point as

$$l_c = (\mathrm{d}V)^{1/3}, \tag{23}$$

where $\mathrm{d}V$ is the volume of concrete represented by the sampling point. Note that this definition does not account for directionality of the cracking or distortion of the element but it can be used as a first-order approximation of the actual control length.

It should be noted that this approach to the computation of the strain-softening branch of the stress–strain curve is only directly applicable to plain concrete. The classical "tension-stiffening" effect due to the presence of reinforcement has not been accounted for. However, the advantages of this approach regarding mesh objectivity for localized fracture are unquestionable. The effect of the reinforcing can be heuristically included by assuming a higher fracture energy for reinforced concrete than for plain concrete.

The redistribution of stresses due to cracking in other sampling point, or further loading, may force some of the previously opened cracks to close partially or fully. This behaviour is allowed in the present model. If the current strain ε is smaller than the strain ε_{ref} recorded as the maximum tensile strain reached across the crack under consideration, the stress normal to the crack, σ, is calculated from

$$\sigma = \frac{\sigma_{ref}}{\varepsilon_{ref}} \varepsilon, \tag{24}$$

in which σ_{ref} is the interpolated stress corresponding to the strain ε_{ref}. This secant "unloading" path is shown in Fig. 9. Re-opening of the crack follows the same path until ε_{ref} is exceeded. Then the stress is interpolated from (21).

(iii) *Shear transfer across the crack.* Experiments show that a considerable amount of shear stress can be transferred across the rough surfaces of cracked concrete. In plain concrete the main shear transfer mechanism is aggregate interlock and the main variables involved are the aggregate size and grading. In reinforced concrete dowel action will play a significant role, the main variables being the reinforcement ratio, the size of the bars and the angle between crack and bars. Both mechanisms are controlled by the width of the crack, the shear transfer capacity being reduced as the width increases.

The above-mentioned mechanisms cannot be directly included in the smeared crack model. A simplified approach is generally employed to take into account the shear transfer capacity of cracked concrete. The process consists of assigning to the shear modulus corresponding to the crack plane a reduced value, G_c, defined as

$$G_c = \beta G_0, \tag{25}$$

where G_0 is the shear modulus of uncracked concrete and β is a reducing factor in the range of zero to one. A constant value for the reducing factor has been used in many analyses. However, it is more realistic to relate the value of β to the tensile strain normal to the crack plane, a smeared measure of the crack width. In this work, the following value is used:

$$\beta = 1 - (\varepsilon_t/0.005)^{k_1}, \tag{26}$$

where ε_t is the fictitious tensile strain normal to the crack plane, and k_1 is a parameter in the range of 0.3–1.0 [25].

Figure 10 shows the variation of β with ε_t for different values of k_1.

Compressive behaviour of cracked concrete. In an earlier section the fact that compressive stresses in the transverse directions reduce the tensile strength of concrete was taken into account in the cracking criterion. The reciprocal effect can also be accounted for: tensile strains in the crack direction effectively reduce the compressive strength in the transverse directions. This effect is included in the present model by scaling the hardening rule described above by a reducing factor [25]

$$\lambda = 1 - k_2 (\varepsilon_t/0.005), \tag{27}$$

where ε_t is the tensile stress normal to the crack plane and k_2 is a factor in the range of 0.1–0.5.

The modified hardening rule is defined by the expression

$$\sigma_0 = -E_0 \varepsilon_p + (2E_0^2 \lambda \varepsilon_0 \varepsilon_p)^{1/2} \lambda \Delta_1 f_c' \leqslant \sigma_0 \leqslant \lambda f_c' \tag{28}$$

and the hardening parameter is given by

$$H' = E_0 [(\lambda \varepsilon_0 / 2\varepsilon_p)^{1/2} - 1]. \tag{29}$$

Figure 11 shows the effect of the scaling of the compressive strength.

Material modelling of the reinforcement. In the present model, the steel reinforcement is smeared into equivalent steel layers with uniaxial properties in the bar direction. In contrast to concrete, the mechanical properties of steel reinforcement are well known. The uniaxial stress–strain curve for steel is idealized in this work as a bilinear curve, representing elastic–plastic behaviour with strain-hardening. The curve is assumed to be identical in tension and compression. Unloading occurs elastically.

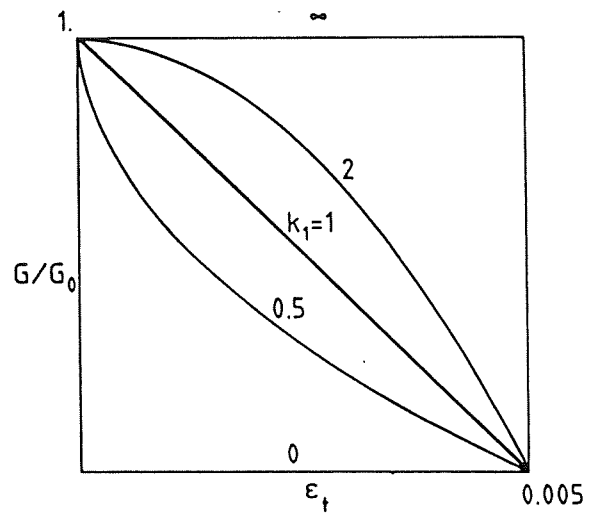

Fig. 10. Variation of the shear modulus with the tensile strain across the crack.

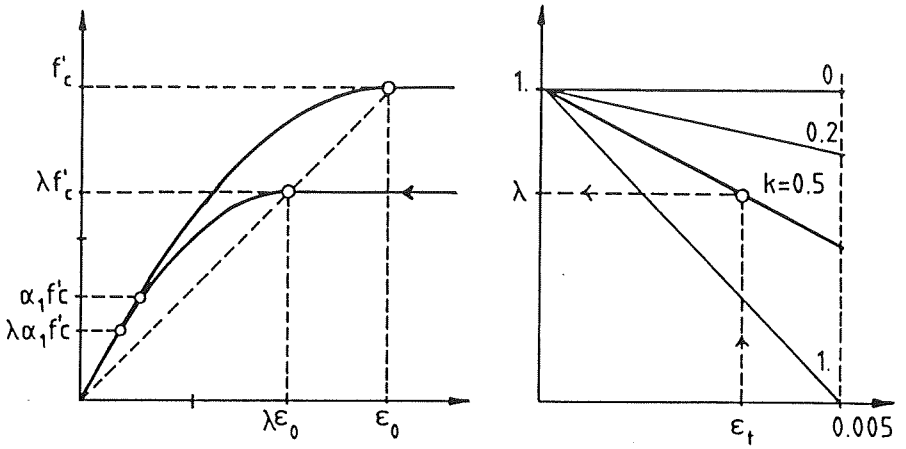

Fig. 11. Reduction of compressive strength due to transverse cracking.

NUMERICAL EXAMPLES

Vecchio–Collins panels

Recently, Vecchio and Collins [26] conducted an excellent study on the behaviour of reinforced concrete panels under in-plane and normal stresses. In their experimental programme they tested 30 specimens of dimensions 890 × 890 × 70 mm (see Fig. 12) on a special testing rig which allowed a uniform plane stress state to be created in the panels. In all cases the reinforcement was arranged parallel to the panel sides, but with different ratios and amounts for different specimens. Of the whole series, only two specimens will be considered here, namely panels 27 and 25. Both have equal reinforcing ratios of 0.01785, in the x and y directions, so they were nominally identical, although the measured concrete properties were slightly different. The material properties used for the numerical analysis are shown in Table 1. Panel 27 was loaded in pure shear, while panel 25 was subjected to a combination of shear and biaxial compression (see Fig. 12). Both panels were loaded proportionally.

The tests are designed so that the response of the panels is mainly dependent on the concrete behaviour. Both panels failed due to crushing of cracked concrete. These examples are included here because they are a demanding test on the computational material model. With one principal stress in tension and the other in compression the problem is designed to test both the tensile and compressive parts of the models, and their mutual influence. It is also interesting to observe how the additional biaxial compression in panel 25 influences the failure load in comparison with panel 27. Although a simple equilibrium analysis shows that the additional compression produces no change in the concrete stress, in reality, panel 25 showed a 44% increase in the shear failure load.

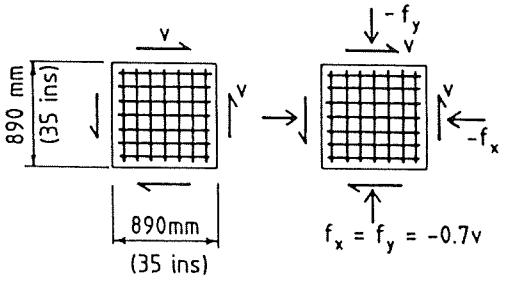

Fig. 12. Dimensions and loads of the Vecchio–Collins panels.

The numerical analyses are performed using the initial stress method, with line search, and a tolerance of 1% on the norm of the residual forces.

Results from the numerical analyses are shown in Figs 13(a) and (b). Excellent agreement between the experimental results and the numerical solution is

Table 1. Material properties for the Vecchio–Collins panels

	Panel 27	Panel 25
Concrete		
Young's modulus	$E_c = 20{,}000.0$	20,000.0 N/mm²
Poisson's ratio	$v = 0.15$	0.15
Ultimate compressive stress	$f'_c = 20.5$	19.3 N/mm²
Ultimate compressive strain	$\varepsilon_{cu} = 0.0035$	0.0035
Cracking tensile stress	$f'_t = 2.4$	2.0 N/mm²
Fracture energy	$G_f = 0.15$	0.15 N/mm²
Shear reduction	$k_1 = 0.4$	0.4
Strength reduction	$k_2 = 0.55$	0.27
Elasticity limit	$\alpha_1 = 0.3$	0.3
Steel		
Young's modulus	$E_s = 200{,}000.0$	200,000.0 N/mm²
Yield stress	$f_y = 442.0$	442.0 N/mm²

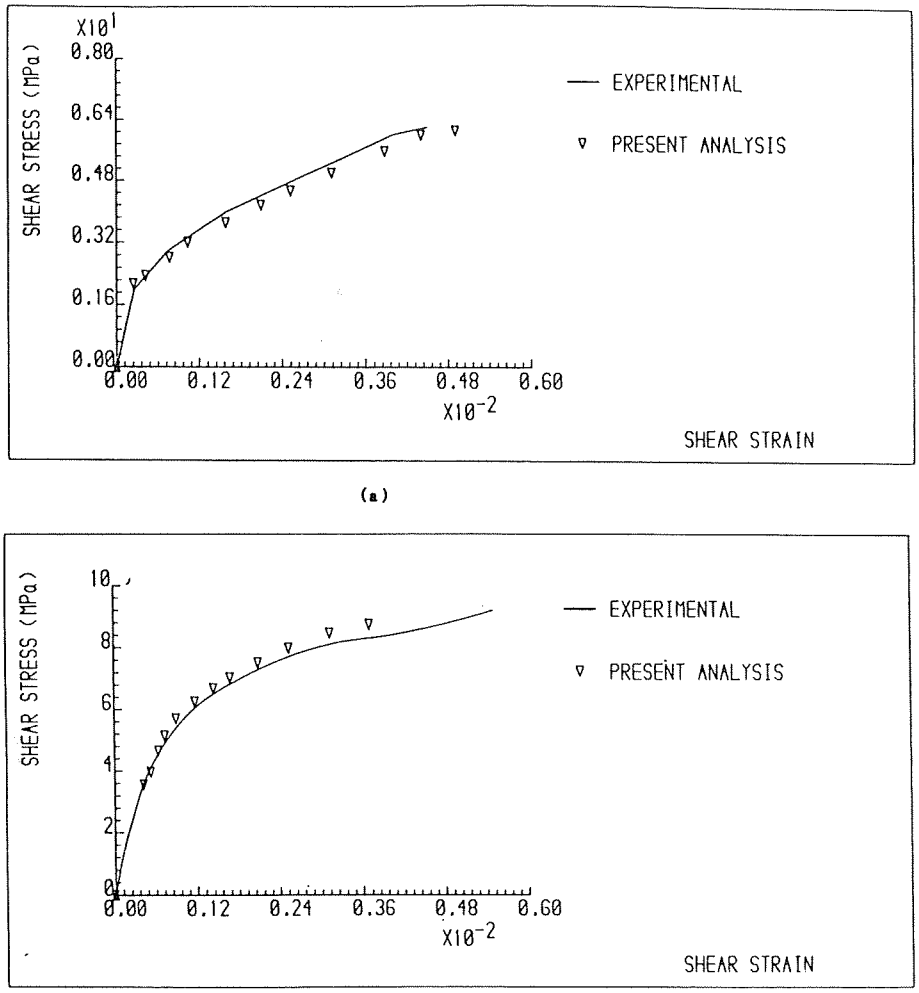

Fig. 13. Shear stress–strain curves for the Vecchio–Collins panels: (a) panel A and (b) panel B.

obtained. Not only are the failure loads accurately predicted in both cases, but the complete stress–strain curves closely agree.

Cardenas–Sozen specimens

In these examples, two rectangular reinforced concrete slabs tested by Cardenas and Sozen [27] are studied. The two specimens, B10 and B7, are tested under uniaxial pure bending. The slabs are almost identical (see Fig. 14) with the only difference being that the reinforcement is parallel to the edges in B10 and oriented at 45° to the edges in B7. The reinforcement consists of four identical layers of bars, each with an equivalent thickness of 0.033 in. The material

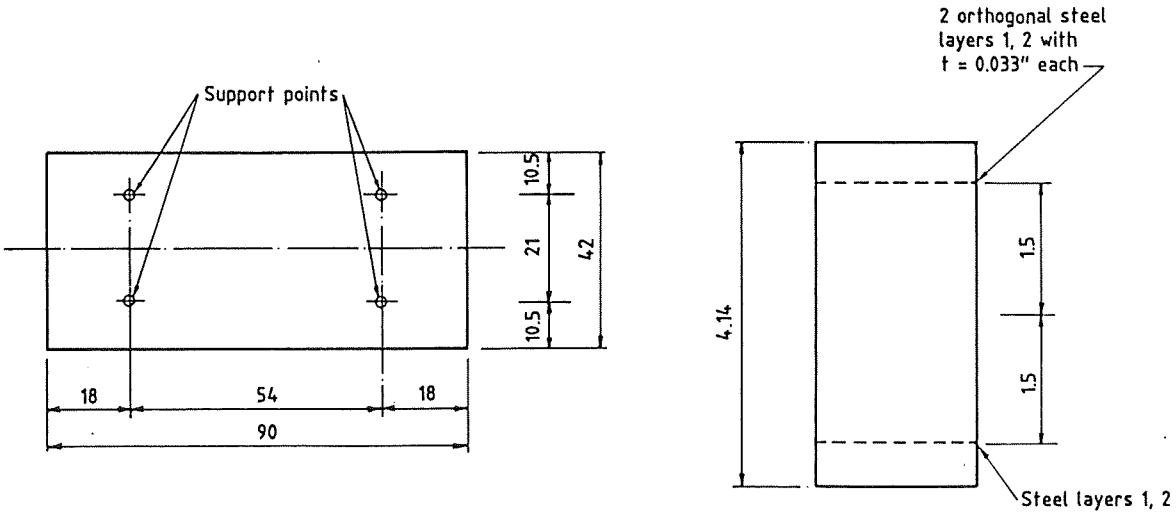

Fig. 14. Geometry and dimensions for the Cardenas–Sozen specimens (all dimensions in inches).

Table 2. Material properties for deep beams

	30-in. beam	20-in. beam
Concrete		
Young's modulus	$E_c = 4600.0$	4600.0 kips/in.^{2}
Poisson's ratio	$\upsilon = 0.17$	0.17
Ultimate compressive stress	$f'_c = 3.96$	2.00 kips/in.^{2}
Ultimate compressive strain	$\varepsilon_{cu} = 0.0035$	0.0035
Cracking tensile stress	$f'_t = 0.36$	0.23 kips/in.^{2}
Fracture energy	$G_f = 0.0006$	0.0006 kips/in.
Shear reduction	$k_1 = 0.5$	0.5
Strength reduction	$k_2 = 0.5$	0.5
Elasticity limit	$\alpha_1 = 0.3$	0.3
Steel		
Young's modulus	$E_s = 29{,}000.0$	29,000.0 kips/in.^{2}
Yield stress	$f_y = 46.0$	46.0 kips/in.^{2}

properties used in the analyses are summarized in Table 2.

In the finite element discretization only one 20-node element is used to represent a symmetric quarter of the constant moment zone (see Fig. 14).

The numerical analysis is done using the KT1 method, with a tolerance of 1% on the norm of the out-of-balance forces.

Comparisons between the experimental and numerical results are shown in Figs 15 and 16. They show moment–steel strain curves for the tension side of the slabs and moment–concrete strain curves for the compression side. Results for specimen B10 agree very well with the experiment. In the numerical solution, concrete strains do not exhibit the final increase at failure because yielding only affects the

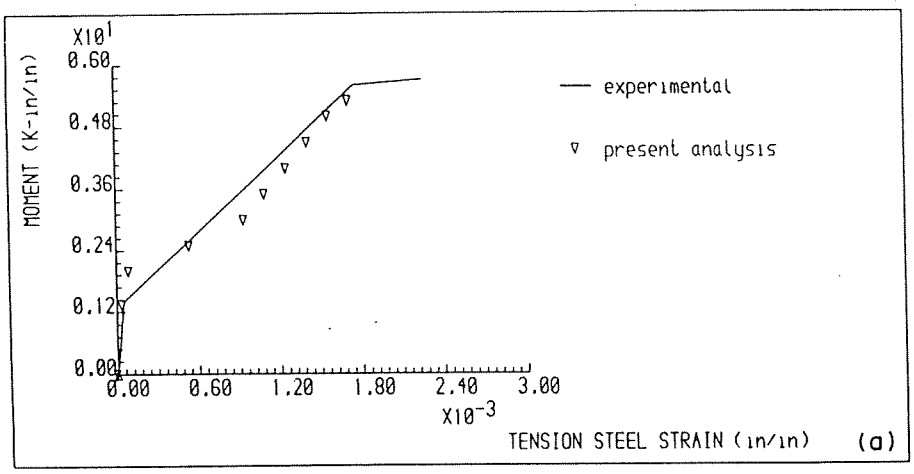

MOMENT-STEEL STRAIN CURVE, TENSION SIDE OF SPECIMEN B7

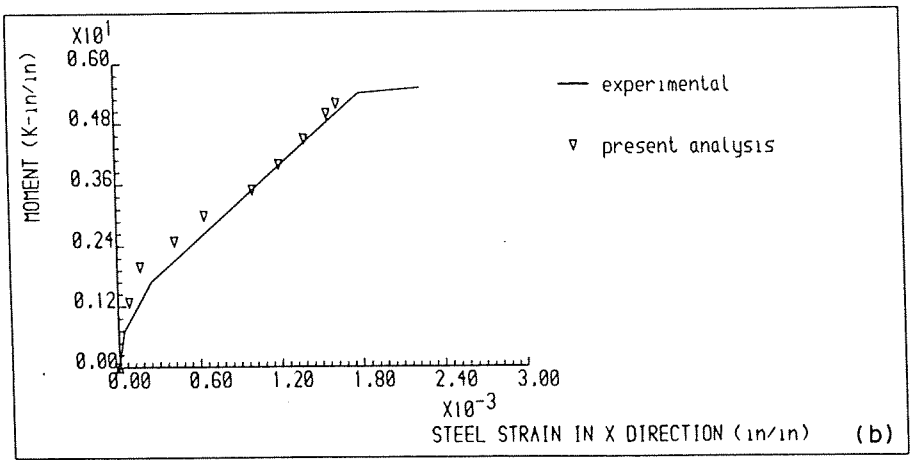

MOMENT-STEEL STRAIN CURVE, TENSION SIDE OF SPECIMEN B10

Fig. 15. Moment–steel strain curves on tension side of Cardenas–Sozen specimens: (a) slab B7 and (b) slab B10.

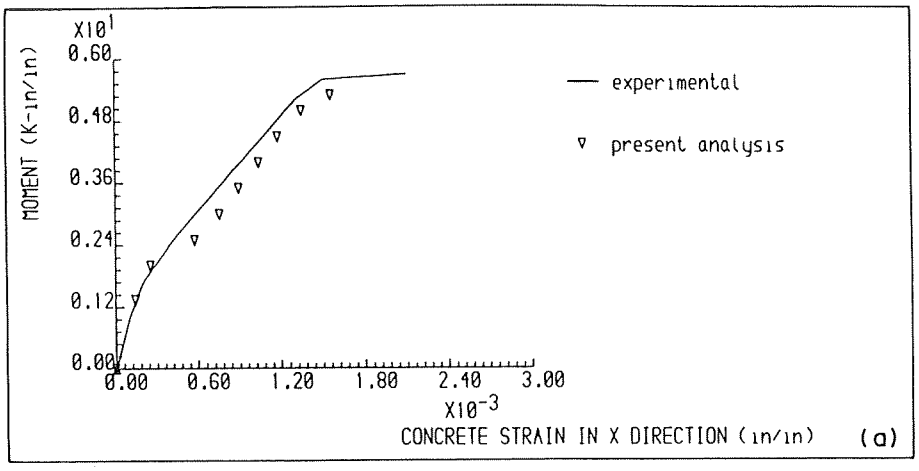

MOMENT-CONCRETE STRAIN CURVE, COMPRESSION SIDE OF SPECIMEN B7

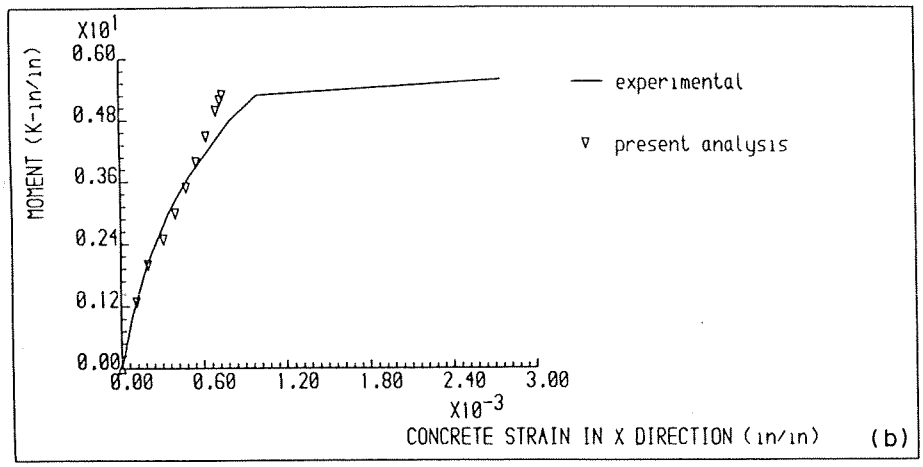

MOMENT-CONCRETE STRAIN CURVE, COMPRESSION SIDE OF SPECIMEN B10

Fig. 16. Moment–concrete strain curves on compression side Cardenas–Sozen specimens: (a) slab B7 and (b) slab B10.

sampling point on the bottom surface, without reaching the next level of points. In specimen B7, a sudden increase in strains occurs, especially in the tension side, because cracking spreads very quickly through the thickness. With the discretization used, this results in a suddent loss of stiffness. Nevertheless, all curves show close agreement with the experiments, with accurate predictions of the cracking and failure loads.

The Bresler–Scordelis beam

The simply supported, reinforced concrete beam tested by Scordelis and Bresler [28] is shown in Fig. 17. This beam has a span of 12 ft with cross-sectional dimensions 21.75 × 9 in. It has no web reinforcement and the longitudinal reinforcement consists of four bars with a total area of 4 in^2.

The beam is subjected to a central concentrated load. The beam fails by crushing of the concrete at the experimentally determined failure load of 58 kips.

The experimental results are considered to be very reliable, so the beam has almost become a standard benchmark for the testing of numerical formulations.

By taking advantage of symmetry only one-half of the beam is idealized with two different meshes: (a) with five equal elements along the span, and (b) with

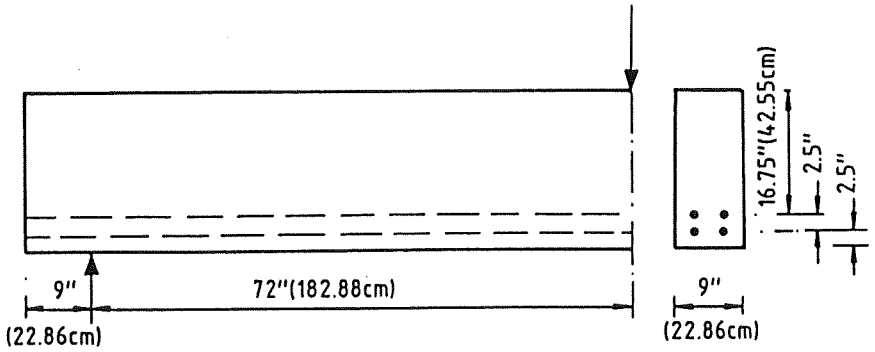

Fig. 17. Bresler–Scordelis beam—geometry and loading.

Table 3. Material properties for the Bresler–Scordelis beam

Concrete	
Young's modulus	$E_c = 3300.0$ kips/in.^{2}
Poisson's ratio	$v = 0.20$
Ultimate compressive stress	$f'_c = 3.16$ kips/in.^{2}
Ultimate compressive strain	$\varepsilon_{cu} = 0.0020$
Cracking tensile stress	$f'_t = 0.33$ kips/in.^{2}
Fracture energy	$G_f = 0.0006$ kips/in.
Shear reduction	$k_1 = 0.5$
Strength reduction	$k_2 = 0.5$
Elasticity limit	$\alpha_1 = 0.3$
Steel	
Young's modulus	$E_s = 27{,}800.0$ kips/in.^{2}
Yield stress	$f_y = 60.0$ kips/in.^{2}

10 equal elements disposed in two layers through the thickness. The material properties used in the analysis are summarized in Table 3.

The numerical analysis is performed using the KT1 method, with a tolerance of 1% on the norm of the residual forces.

In Fig. 18 the experimental load–deflection curve at the midspan section of the beam is compared with the curves predicted in analyses based on the two meshes. From this it can be seen that both meshes give very similar results, despite the reduction of the element size. Both numerical solutions are in close agreement with the experiment. The failure load for mesh (a) is 61.71 kips (6.4% error) and for mesh (b) the failure load is 58.84 (1.4% error).

Crack patterns for different load intensities are plotted in Fig. 19. Note that for the 3-D analyses cracks are represented as flat squares in the physical crack plane. The distortion of the squares gives an idea of the inclination of the cracks. Only two orthogonal cracks are allowed to open at each sampling point. When two non-orthogonal cracks appear at a point in one of the figures, or more than two cracks are present, this is because that particular point is actually two sampling points for two adjacent elements and cracks in both elements are plotted at the same position.

The behaviour of the numerical model agrees well with the reported experimental observations. Cracks start to develop at the midspan of the beam, where tensile stresses are larger. They spread gradually along the span and through the thickness. The cracks observed at the top of the beam are caused by the reduction of the tensile strength due to the high compressive stresses in that region. In the latest stages

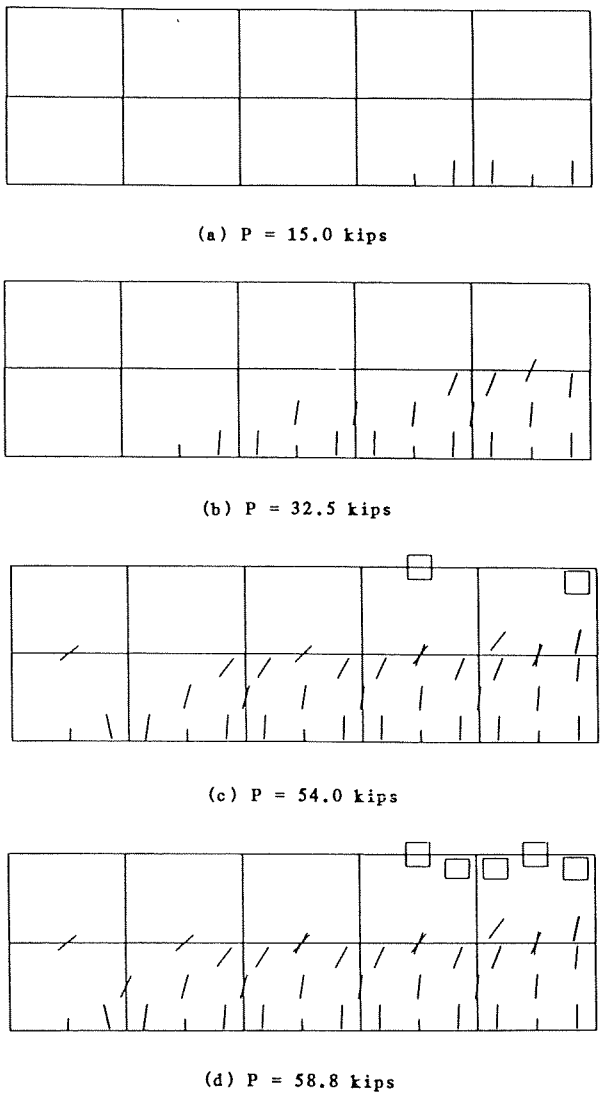

Fig. 19. Crack patterns for Bresler–Scordelis beam at different stages of loading.

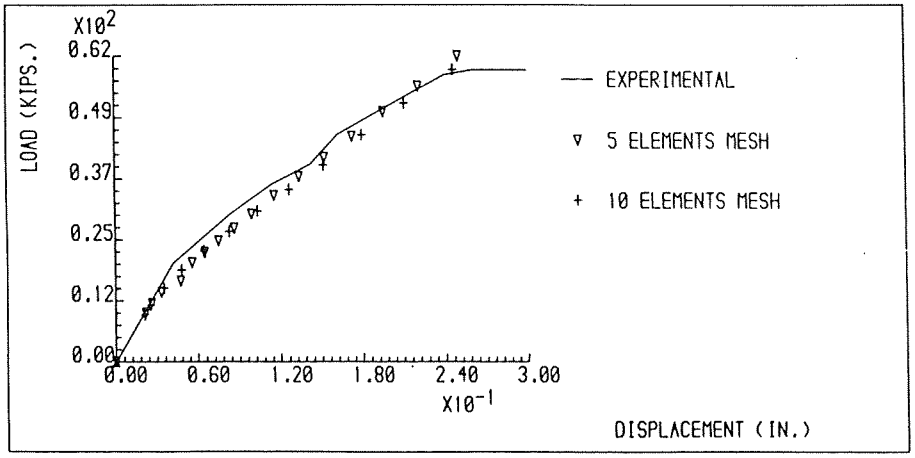

Fig. 18. Load–displacement curve for Bresler–Scordelis beam.

Table 4. Material properties for the Duddeck's slabs

Concrete	
Young's modulus	$E_c = 16{,}400.0$ N/mm^2
Poisson's ratio	$\nu = 0.15$
Ultimate compressive stress	$f'_c = 43.0$ N/mm^2
Ultimate compressive strain	$\varepsilon_{cu} = 0.0035$
Cracking tensile stress	$f'_t = 3.0$ N/mm^2
Fracture energy	$G_f = 0.200$ N/mm
Shear reduction	$k_1 = 1.0$
Strength reduction	$k_2 = 0.0$
Elasticity limit	$\alpha_1 = 0.3$
Steel	
Young's modulus	$E_s = 201{,}000.0$ N/mm^2
Yield stress	$f_y = 670.0$ N/mm^2

of the analysis most of the bottom half of the beam is cracked and the diagonal cracks typical of this geometry and loading are evident. The dominant diagonal crack that was reported to be responsible for the experimental failure was probably caused by the excessive deformation that occurs after crushing of the concrete starts.

Duddeck's slabs

In this example three corner-supported slabs tested by Duddeck *et al.* [29] are studied. These slabs have various degrees of orthotropy of the steel reinforcement. This example has the advantage of well-defined support conditions. Only transverse deflections are restrained at the corner supports.

The material properties are rather poorly defined. The values assumed here are summarized in Table 4. The equivalent reinforcement layers for the three slabs are given below in millimetres:

	Top layers		Bottom layers	
	x-dir	y-dir	x-dir	y-dir
S1	0.193	0.193	0.397	0.397
S2	0.252	0.133	0.520	0.273
S3	0.283	0.103	0.582	0.212

All three slabs were tested under the same loading conditions of a concentrated load at the slab centre.

In the finite element analysis, by taking advantage of symmetry, it is only necessary to consider one-quarter of the slab. A $3 \times 3 \times 1$ mesh of 20-node elements is adopted, as shown in Fig. 20. The mesh is refined near the centre of the slab, where higher stresses are expected due to the application of the central point load.

The analyses are performed using the arc-length method with the spherical path formulation. A tolerance of 1% on the norm of the residual forces is used.

The failure loads (expressed in kiloNewtons) obtained in the numerical analyses are now listed, and compared with the experimental values and the predictions obtained using yield line theory.

	Numerical	Experimental	Error (%)	Yield line
S1	59.61	61.06	−3.32	56.00
S2	45.05	43.46	+3.66	39.24
S3	36.29	34.25	+5.95	30.76

Excellent agreement with the experiments is observed for the failure loads and it is also found throughout the whole loading process as can be seen from the load–central deflection curves of Figs 21(a)–(c). The crack patterns obtained for the bottom surface (tension side) at different load levels are shown in Figs 22(a)–(c). It can be seen that cracks spread throughout most of the three slabs. This causes the nonlinear behaviour in the early stages. Failure is ultimately caused by yielding of the reinforcement. This is why such a reduction of the failure loads is observed when the reinforcement is not disposed isotropically. The arrangement of the reinforcement also affects the direction of the cracks, particularly those which form later.

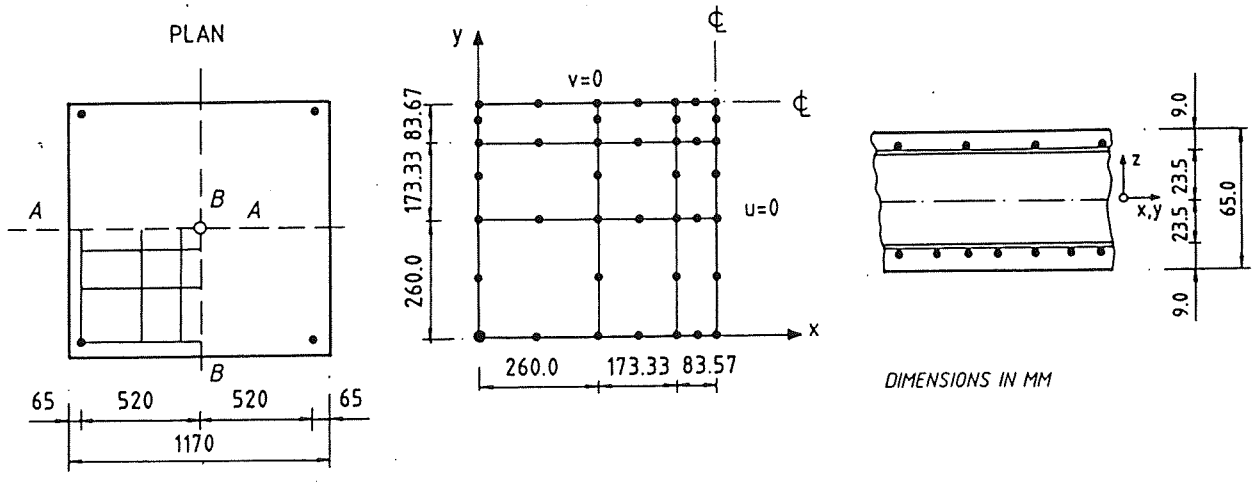

Fig. 20. Structure and idealization of Duddeck's slabs.

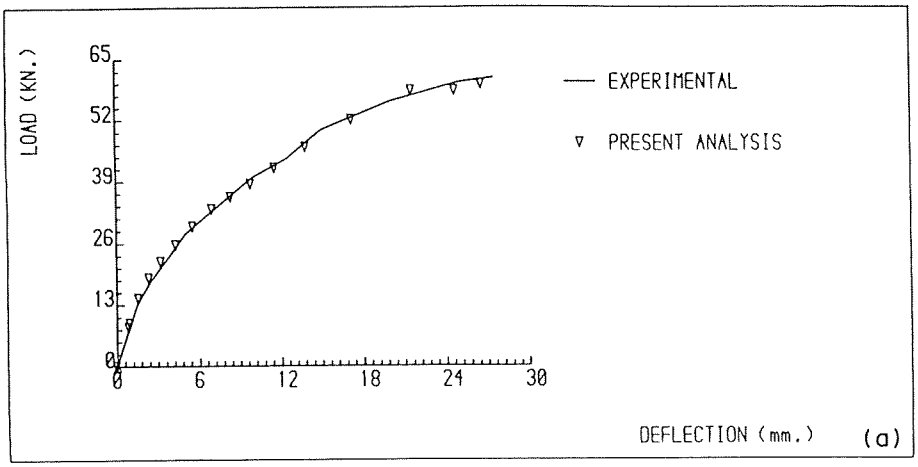

LOAD DEFLECTION CURVE FOR DUDDECK'S SLAB S1

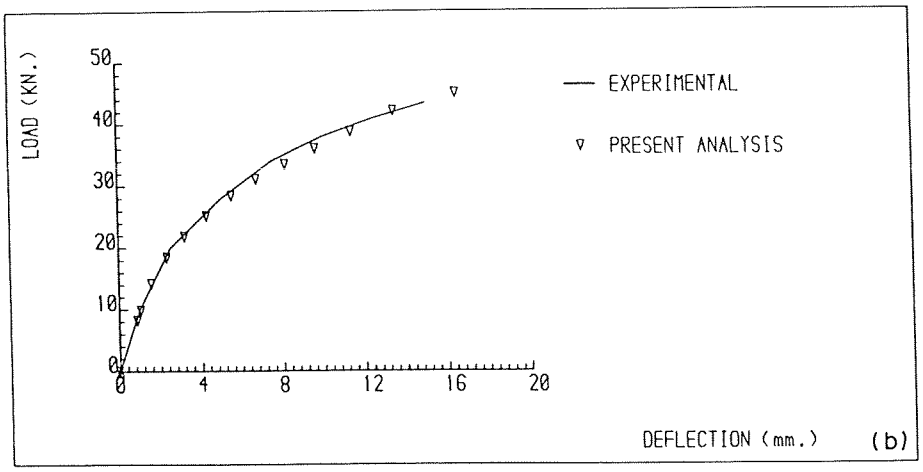

LOAD-DEFLECTION CURVE FOR DUDDECK'S SLAB S2

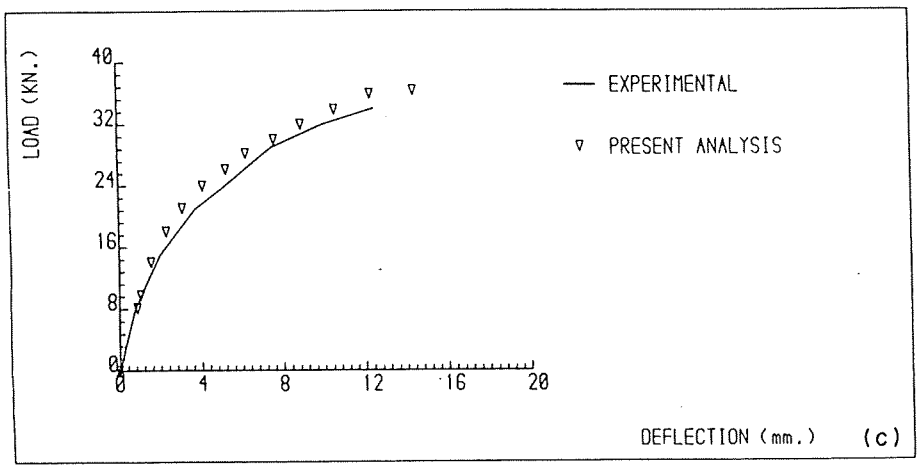

LOAD-DEFLECTION CURVE FOR DUDDECK'S SLAB S3

Fig. 21. Central load–deflection curves for Duddeck's slabs: (a) slab S1, (b) slab S2 and (c) slab S3.

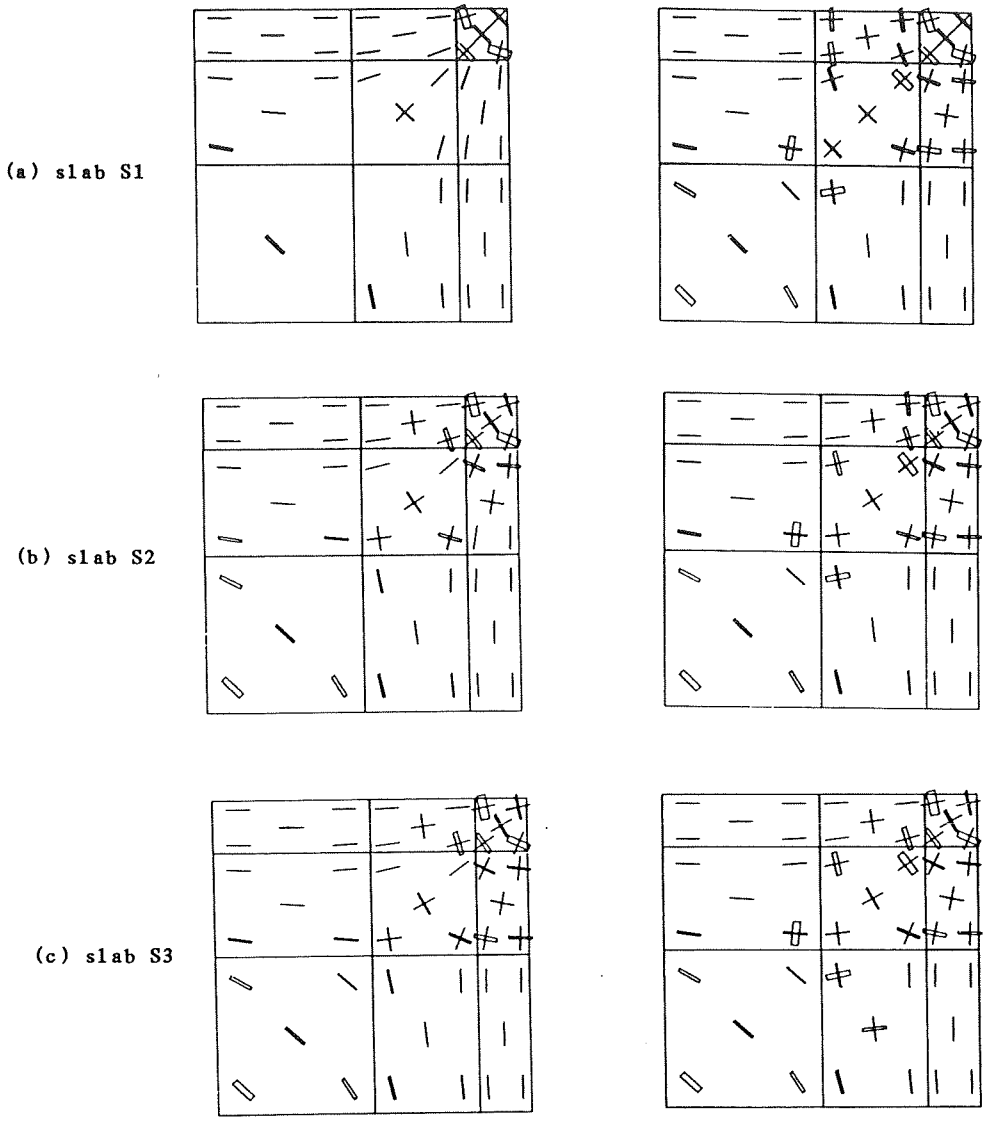

Fig. 22. Crack patterns for Duddeck's slabs: (a) crack patterns for slab S1 at loads $P = 22$ kN and 37 kN, (b) crack patterns for slab S2 at loads $P = 25$ kN and 36 kN and (c) crack patterns for slab S3 at loads $P = 26$ kN and 36 kN.

Illinois slab–column connection tests

In this example, two tests from a series carried out by Sunidja *et al.* [30] at the University of Illinois in Urbana–Champaign are studied. The object of these tests was to study the strength and behaviour of unbonded prestressed concrete plate–edge column connections representative of those used in prestressed flat-plate buildings and subjected to static vertical loading.

The test specimens consist of a 1524-mm square prestressed concrete slab, 101.6 mm in total thickness and with a 304.8-mm square column located adjacent to and centred along one edge of the slab. The system and the dimensions of the slab are shown in Fig. 23.

The two-way flat slabs are prestressed in both directions. The arrangement of the tendons is shown in Fig. 24. In addition, No. 3 deformed bars (71 mm cross-sectional area) are used as bonded reinforcement, as shown in Fig. 23.

The slabs are loaded by four concentrated loads placed at a distance of 1066.8 mm from the column face for slab S1 and 609.6 mm for slab S2.

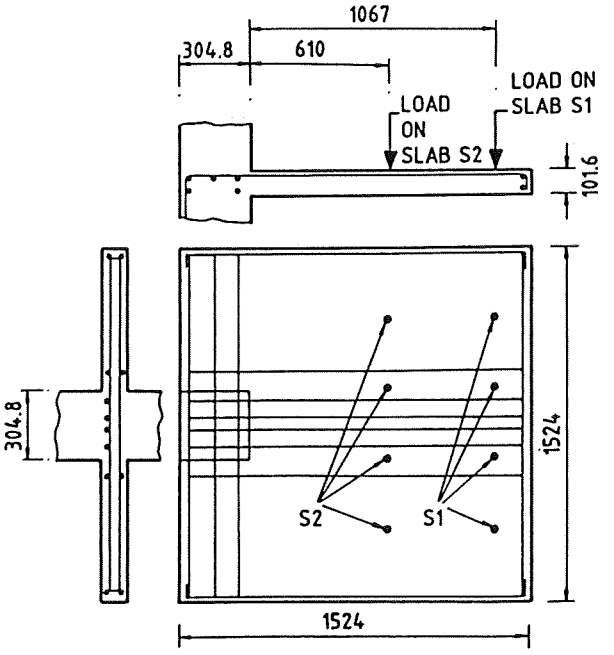

Fig. 23. Illinois slab–column connection tests—geometry, bonded reinforcement layout and loadings.

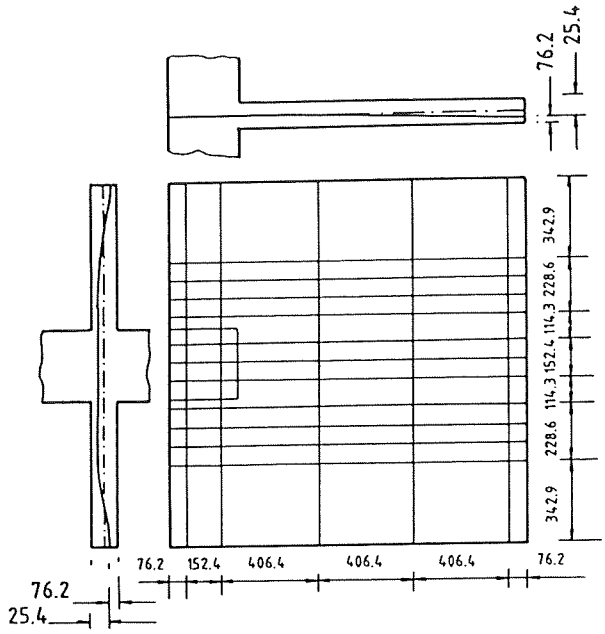

Fig. 24. Illinois slab–column connection tests—unbonded tendons.

By taking advantage of symmetry only one-half of the slab is discretized in each analysis. The slabs are assumed to be clamped at the column edge. This assumption is justfied because the heavily reinforced column is very stiff when compared to the slab.

Both analyses are performed using the KT1 method with line search. A tolerance of 1% on the norm of the residual forces is adopted.

The pre-tension forces are represented by a horizontal load at the slab edges, as shown in Fig. 25. To account for the pre-tension forces due to the curvature of the tendons, additional lateral forces are applied to the slabs, as shown in Fig. 25. In the analysis the pre-tension and the self-weight load of 25,000 N/mm^2 are applied as initial loads and kept constant during the incrementation of the concentrated loads.

The results and meshes used for the analyses can be seen in Figs 26–28. Both meshes consist of twenty 20-node elements.

The material properties used for the analyses are summarized in Table 5.

In Fig. 26 the moment–deflection relations obtained from the numerical computations are compared with the test results. The moment is obtained by multiplying the total applied load by the distance from the load to the face of the column. The initial moment caused by the self-weight of the slab is 288 kN cm. The deflections shown are the additional values due to the concentrated loads and do not include the deformation caused by either the dead load or the pre-tension. The deflection is measured at the east edge of the slab, and on the axis of symmetry.

In the experiment, slab S1 failed in a flexural mode, while slab S2 collapsed due to a dominant shear crack. Figure 26(a) shows that both the initial stiffness and the progressively nonlinear response of slab S1 are accurately predicted by the analysis. The failure load is very well predicted. Results for slab S2, shown in Fig. 26(b), are also in close agreement with the experiment, although a slightly less ductile behaviour at failure than in the experiment is observed.

Figures 27 and 28 show the spread of the cracking on the tension side of the slabs (top surfaces) for different load levels. As expected, cracking is mostly confined to the part of the slabs between the support and the locations of the loads. In both cases, cracks start to form close to the column, where tensile stresses are larger, and gradually spread towards

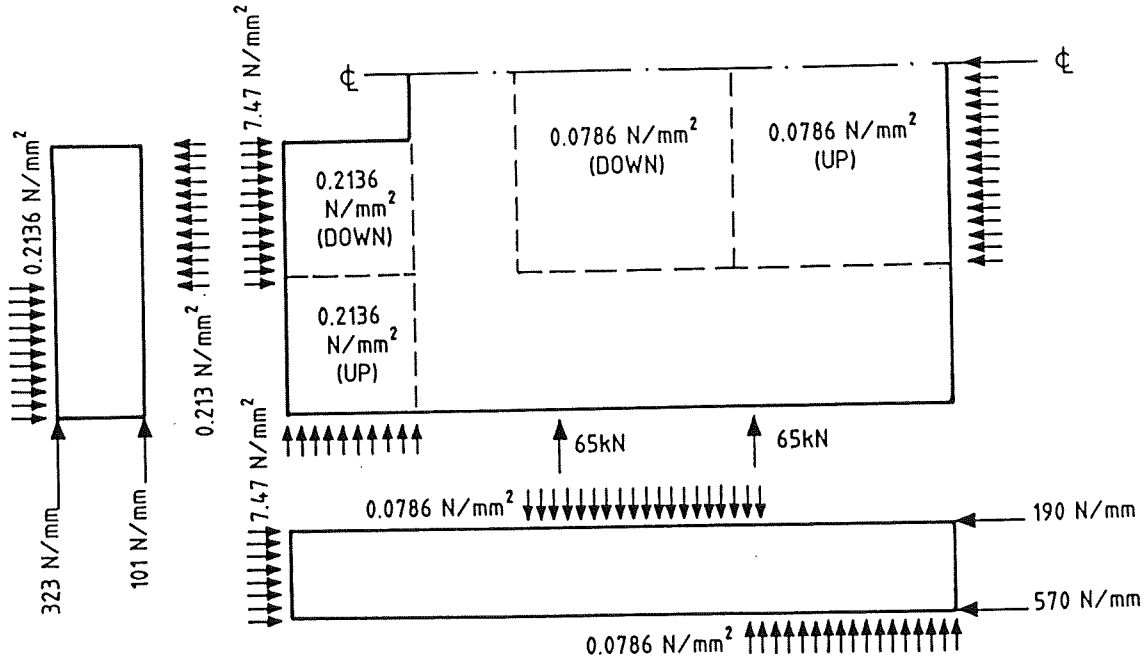

Fig. 25. Illinois slab–column connection tests—load pattern applied to model pre-tension forces.

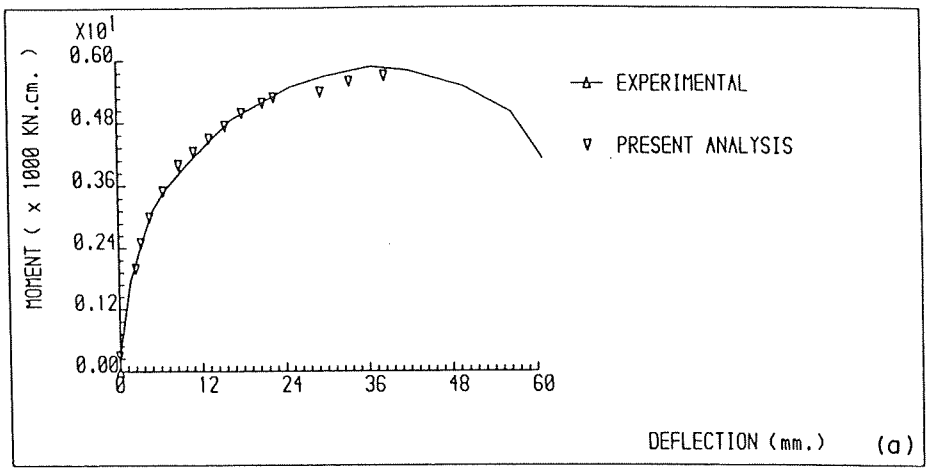

LOAD-DEFLECTION CURVE FO ILLINOIS SLAB S1

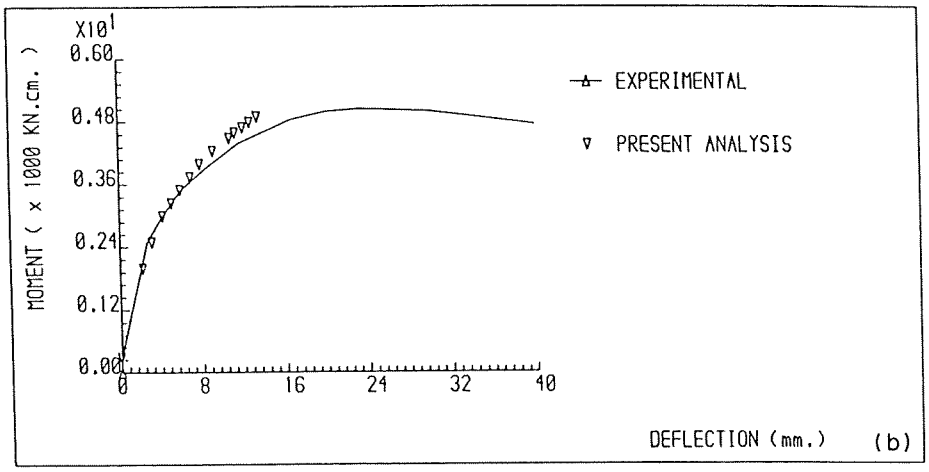

LOAD-DEFLECTION CURVE FOR ILLINOIS SLAB S2

Fig. 26. Moment–deflection curves for Illinois slab–column connection tests: (a) slab S1 and (b) slab S2.

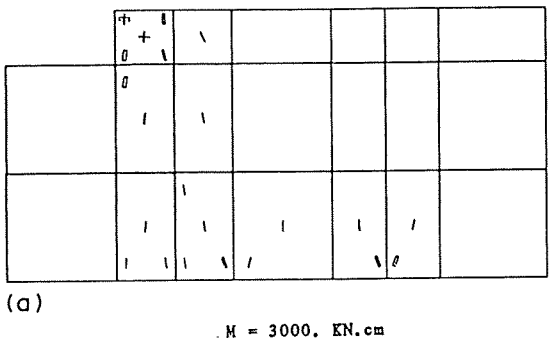

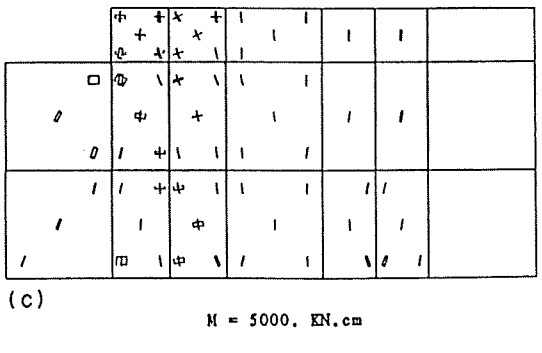

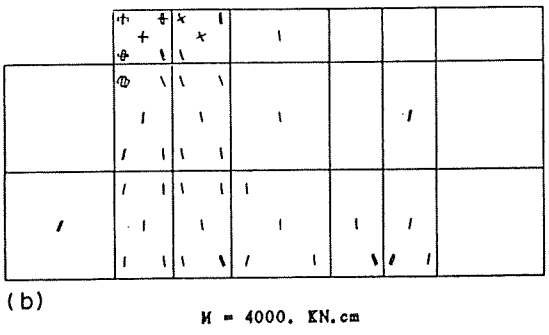

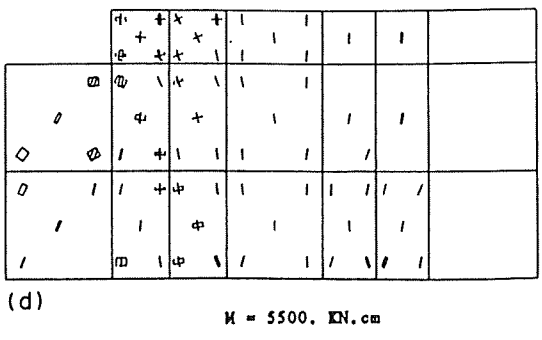

Fig. 27. Crack patterns for Illinois slab–column connection test slab S1 at various applied moment levels: (a) $M = 3000$ kN cm, (b) $M = 4000$ kN cm, (c) $M = 5000$ kN cm and (d) $M = 5500$ kN cm.

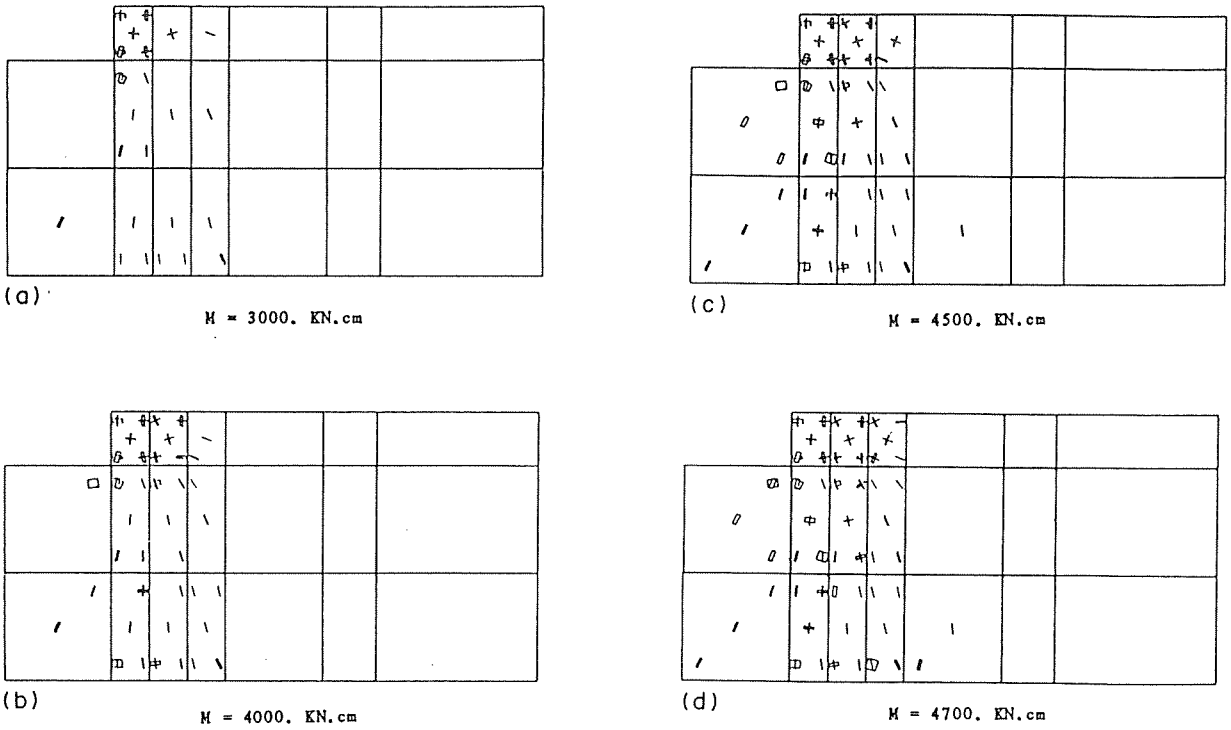

Fig. 28. Crack patterns for Illinois slab–column connection test slab S2 at various applied moment levels: (a) $M = 3000$ kN cm, (b) $M = 4000$ kN cm, (c) $M = 4500$ kN cm and (d) $M = 4700$ kN cm.

Table 5. Material properties for the Illinois slab–column

	S1	S2
Concrete		
Young's modulus	$E_c = 29{,}000.0$	24,000.0 N/mm^2
Poisson's ratio	$v = 0.15$	0.15
Ultimate compressive stress	$f'_c = 50.0$	43.0 N/mm^2
Ultimate compressive strain	$\varepsilon_{cu} = 0.0035$	0.0035
Cracking tensile stress	$f'_t = 3.67$	3.15 N/mm^2
Fracture energy	$G_f = 0.10$	0.10 N/mm
Shear reduction	$k_1 = 0.50$	0.50
Strength reduction	$k_2 = 0.50$	0.50
Elasticity limit	$\alpha_1 = 0.30$	0.30
Steel		
Young's modulus	$E_s = 200{,}000.0$	200,000.0 N/mm^2
Yield stress	$f_y = 500.0$	500.0 N/mm^2

Table 6. Material properties for deep beams

	30-in. beam	20-in. beam
Concrete		
Young's modulus	$E_c = 4600.0$	4600.0 kips/in.^{2}
Poisson's ratio	$v = 0.17$	0.17
Ultimate compressive stress	$f'_0 = 3.96$	2.00 kips/in.^{2}
Ultimate compressive strain	$\varepsilon_{cu} = 0.0035$	0.0035
Cracking tensile stress	$f'_t = 0.36$	0.23 kips/in.^{2}
Fracture energy	$G_f = 0.0006$	0.0006 kips/in.
Shear reduction	$k_1 = 0.5$	0.5
Strength reduction	$k_2 = 0.5$	0.5
Elasticity limit	$\alpha_1 = 0.3$	0.3
Steel		
Young's modulus	$E_s = 29{,}000.0$	29,000.0 kips/in.^{2}
Yield stress	$f_y = 46.0$	46.0 kips/in.^{2}

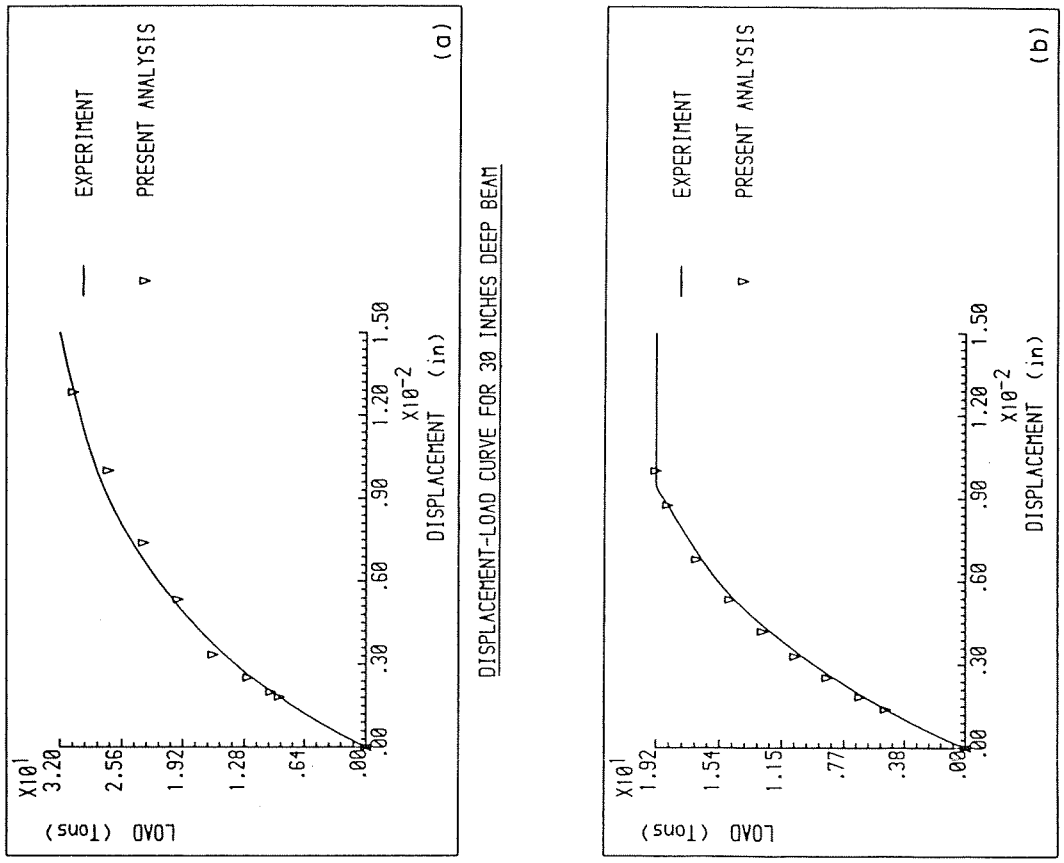

Fig. 30. Load–deflection curves for deep beams: (a) 30-in. deep beam and (b) 20-in. deep beam.

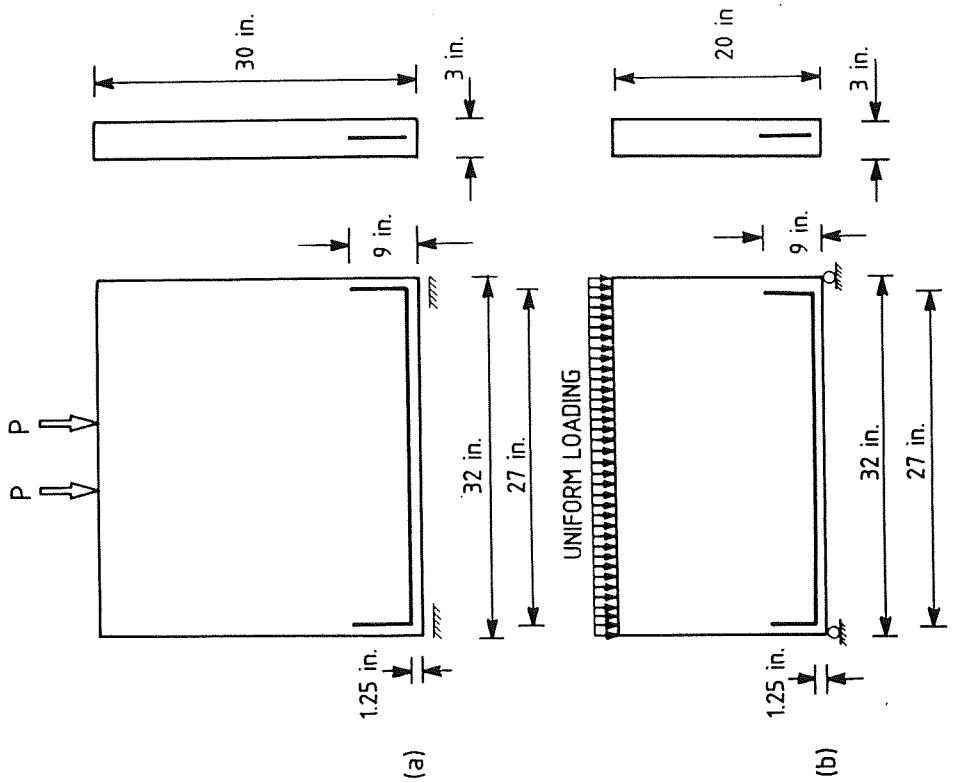

Fig. 29. Deep beam problems (Ramakrishan and Anatha-narayana): geometry, loading and reinforcement: (a) 30-in. deep beam and (b) 20-in. deep beam.

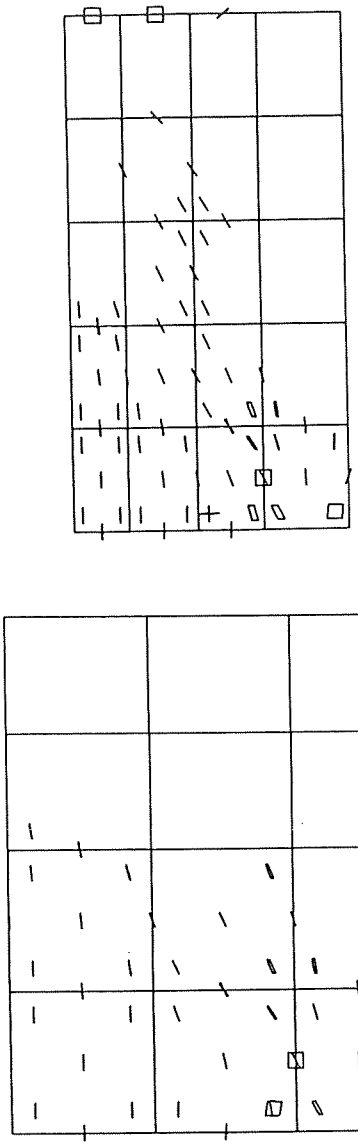

Fig. 31. Crack patterns for deep beams: (a) 30-in. deep beam and (b) 20-in. deep beam.

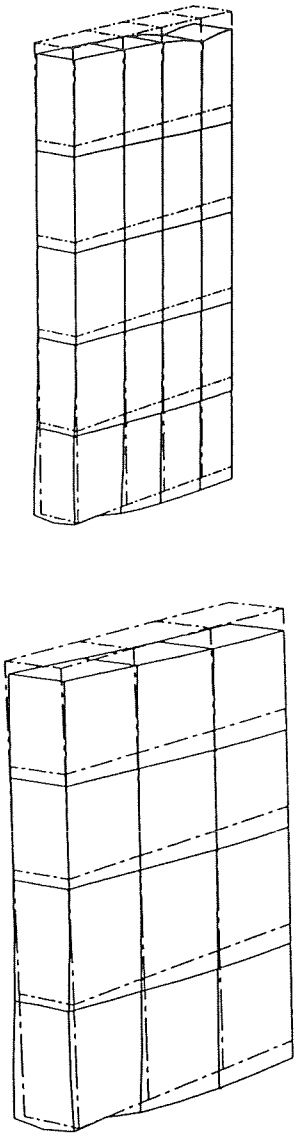

Fig. 32. Deformed meshes for deep beams: (a) 30-in. deep beam and (b) 20-in. deep beam.

the loads and through the thickness. Some double-cracking is observed around the column in both cases.

Analysis of deep beams

In this final example, two deep beams experimentally studied by Ramakrishan and Anathanarayana [31] are analysed. One beam is 30 in. and the other 20 in. deep. The first is subjected to two point loads, while the other is loaded with a uniform pressure (see Fig. 29). The reinforcement consists of one bar of cross-section 1 in.^{2} The material properties used in the analysis are shown in Table 6.

By taking advantage of symmetry, only one-half of the beams is discretized, using meshes of 12 and 20 elements.

The analyses are performed using the initial stress method, with a tolerance of 1% on the norm of the residual forces.

Load–deflection curves are shown in Fig. 30. Excellent agreement with the experimental results is obtained. The ultimate loads are also accurately predicted.

The computed crack patterns at failure are shown in Figs 31(a) and (b). The experimentally observed cracks (a stable flexural crack at mid-span and an unstable one running from the loads towards the support) are well predicted in the numerical analysis. Deformed shapes at failure are shown in Fig. 32.

REFERENCES

1. O. C. Zienkiewicz, J. P. S. E. Gago and D. W. Kelly, The hierarchical concept in finite element analysis. *Comput. Struct.* **16**, (1983).
2. D. Koslov and G. A. Frazier, Treatment of hourglass patterns in low order finite element codes. *Int. numer. Anal. Meths Geom.* (1978).
3. D. P. Flanagan and T. Belytschko, A uniform strain hexahedron and quadrilateral with orthogonal hourglass control. *Int. J. numer. Meths Engng* **17**, (1981).
4. M. A. Crisfield, Some recent research on numerical techniques for structural analysis. *NUMETA* 85, 565–575 (1985).

5. B. M. Irons, Quadrature rules for brick-based finite elements. *Int. J. numer. Meths Engng* **3,** 293–294 (1971).
6. O. Buyukozturk and S. S. Shareef, Constitutive modeling of concrete in finite element analysis. *Comput. Struct.* **21,** 581–610 (1985).
7. D. V. Phillips and O. C. Zienkiewicz, Finite element nonlinear analysis of concrete structures. *Proc. Inst. civ. Engng* **61,** 59–98 (1976).
8. O. C. Zienkiewicz, D. R. J. Owen and D. V. Phillips, Finite element analysis of reactor vessels. *Nucl. Engng Design* **20,** 507–541 (1972).
9. D. R. J. Owen and J. A. Figueiras, Ultimate load analysis of reinforced concrete plates and shells including geometric nonlinear effects. In *Finite Element Software for Plates and Shells* (Edited by E. Hinton and D. R. J. Owen). Pineridge Press, Swansea (1984).
10. H. Kupfer, K. H. Hilsdorf and H. Rush, Behaviour of concrete under biaxial stresses. *Proc. ACI* **66** (8), 656–666 (1969).
11. D. R. J. Owen and E. Hinton, *Finite Element in Plasticity—Theory and Practice.* Pineridge Press, Swansea (1980).
12. R. J. Cope, P. V. Rao, L. A. Clark and P. Norris, Modelling of reinforced concrete behaviour for finite element analysis of bridge decks. In *Proc. Int. Conf. Numer. Meths for Non-Linear Problems.* (Edited by C. Taylor *et al.*). Pineridge Press, Swansea (1980).
13. Z. P. Bazant, Discussion on Session 2—Structural modelling for numerical analysis. IABSE Colloq., Final Rep. 482, Delft (1981).
14. A. Scanlon and D. W. Murray, Time-dependent reinforced concrete slab deflections. *J. struct. Div., ASCE* **100,** 1911–1924 (1974).
15. R. I. Gilbert and R. F. Warner, Tension stiffening in reinforced concrete slabs. *J. struct. Div., ASCE* **104,** 1885–1900 (1978).
16. A. Hillerborg, H. Modeer and P. E. Petersson, Analysis of crack formation and crack growth in concrete by means of fracture mechanics and finite elements. *Cement Concrete Res.* **6,** 773–781 (1976).
17. Z. P. Bazant and L. Cedolin, Fracture mechanics of reinforced concrete. *J. mech. Div., ASCE* **106,** 1207–1306.
18. K. J. Willam and S. Sture, A composite fracture model for localized fracture in cementitious materials. Second Symp. on the interaction of non-nuclear munitions with structures, Florida (1985).
19. K. J. Willam, Experimental and computational aspects of concrete fracture. In *Computer-aided Analysis and Design of Concrete Structures* (Edited by F. Damjanic *et al.*), pp. 33–70. Pineridge Press, Swansea (1984).
20. K. J. Willam, N. Bicanic and S. Sture, Constitutive and computational aspects of strain-softening and localization in solids. ASME-WAM '84 Symp. Constitutive equations: micro, macro and computational aspects, New Orleans (1984).
21. P. E. Petersson, Crack growth and development of fracture zones in plain concrete and similar materials. Ph.D. thesis, University of Lund (1981).
22. L. Nilsson and M. Oldenburg, Nonlinear wave propagation in plastic fracturing materials—a constitutive modelling and finite element analysis. IUTAM Symp. Nonlinear Deformation Waves, Tallin (1982).
23. J. J. Jiang, Finite element techniques for statistical analysis of structures in reinforced concrete. Ph.D. thesis, Department of Structural Mechanics, Chalmers University of Technology (1983).
24. R. Glemberg, Dynamic analysis of concrete structures. Ph.D. thesis, Department of Structural Mechanics, Chambers University of Technology (1984).
25. V. Cervenka, Constitutive model for cracked reinforced concrete. *ACI Jnl* **82,** 877–882 (1985).
26. F. Vecchio and M. P. Collins, The response of reinforced concrete to in-plane shear and normal stress. Publ. No. 82–03, Department of Civil Engineering, University of Toronto (1982).
27. A. Cardenas and M. A. Sozen, Strength and behaviour of isotropically and nonisotropically reinforced concrete slabs subjected to combinations of flexural and torsional moments. Civil Engineering Studies, SRS No. 336, University of Illinois, Urbana (1968).
28. H. A. Franklin, Nonlinear analysis of reinforced concrete frames and panels. Report No. SESM 70–5, Department of Civil Engineering, University of California, Berkeley (1970).
29. H. Duddeck, G. Griebow and G. Schaper, Material- and time-dependent nonlinear behaviour of cracked concrete slabs. In *Nonlinear Behaviour of Reinforced Concrete Spatial Structures,* Vol. 1. Preliminary Report, IASS Symp., Darmstadt (1978).
30. H. Sunidja, D. A. Foutch and W. L. Gamble, Response of prestressed concrete plate-edge column connections. Civil Engng Studies, Struct. Res., Ser. No. 498, University of Illinois, Urbana–Champaign (1982).
31. V. Ramakrishan and Y. Anathanarayana, Ultimate strength of deep beams in shear. *ACI Jnl* **65,** 87–98 (1968).